

The multi-messenger picture of compact object encounters: binary mergers versus dynamical collisions

S. Rosswog^{1,2,3*}, T. Piran^{4†} and E. Nakar^{5‡}

¹*School of Engineering and Science, Jacobs University Bremen, Germany*

²*TASC, Department of Astronomy and Astrophysics, University of California, Santa Cruz, CA 95064*

³*The Oskar Klein Centre, Department of Astronomy, AlbaNova, Stockholm University, SE-106 91 Stockholm, Sweden*

⁴*Racah Institute of Physics, The Hebrew University, Jerusalem 91904, Israel*

⁵*Raymond and Beverly Sackler School of Physics & Astronomy, Tel Aviv University, Tel Aviv 69978, Israel*

Accepted 2012. Received 2012; in original form 2012

ABSTRACT

We explore the multi-messenger signatures of encounters between two neutron stars (ns^2) and between a neutron star and a stellar-mass black hole (nsbh). We focus on the differences between gravitational wave driven binary mergers and dynamical collisions that occur, for example, in globular clusters. Our discussion is based on Newtonian hydrodynamics simulations that incorporate a nuclear equation of state and a multi-flavour neutrino treatment. For both types of encounters we compare the gravitational wave and neutrino emission properties. We also calculate the rates at which nearly unbound mass is delivered back to the central remnant in a ballistic-fallback-plus-viscous-disk model and we analyze the properties of the dynamically ejected matter. Last but not least we address the electromagnetic transients that accompany each type of encounter.

We find that dynamical collisions are at least as promising as binary mergers for producing (short) gamma-ray bursts, but they also share the same possible caveats in terms of baryonic pollution. All encounter remnants produce peak neutrino luminosities of at least $\sim 10^{53}$ erg/s, some of the collision cases exceed this value by more than an order of magnitude. The canonical ns^2 merger case ejects more than 1% of a solar mass of extremely neutron-rich ($Y_e \sim 0.03$) material, an amount that is consistent with double neutron star mergers being a major source of r-process in the galaxy. nsbh collisions eject very large amounts of matter ($\sim 0.15 M_\odot$) which seriously constrains their admissible occurrence rates. The compact object *collision* rate (sum of ns^2 and nsbh) must therefore be less, likely much less, than 10% of the ns^2 *merger* rate. The radioactively decaying ejecta produce optical-UV “macronova” which, for the canonical merger case, peak after ~ 0.4 days with a luminosity of $\sim 5 \times 10^{41}$ erg/s. ns^2 (nsbh) collisions reach up to 2 (4) times larger peak luminosities. The dynamic ejecta deposit a kinetic energy comparable to a supernova in the ambient medium. The canonical merger case releases approximately 2×10^{50} erg, the most extreme (but likely rare) cases deposit kinetic energies of up to 10^{52} erg. The deceleration of this mildly relativistic material by the ambient medium produces long lasting radio flares. A canonical ns^2 merger at the detection horizon of advanced LIGO/Virgo produces a radio flare that peaks on a time scale of one year with a flux of ~ 0.1 mJy at 1.4 GHz. Collisions eject more material at higher velocities and therefore produce brighter and longer lasting flares.

Key words: black hole physics – gravitational waves – neutrinos – nuclear reactions, nucleosynthesis, abundances – radiation mechanisms: non-thermal— gamma-ray bursts

1 INTRODUCTION

The encounter of a neutron star (ns) with another neutron star or with a stellar mass black hole (bh) is a fascinating

* E-mail: s.rosswog@jacobs-university.de

† E-mail: tsvi.piran@mail.huji.ac.il

‡ E-mail: udini@wise.tau.ac.il

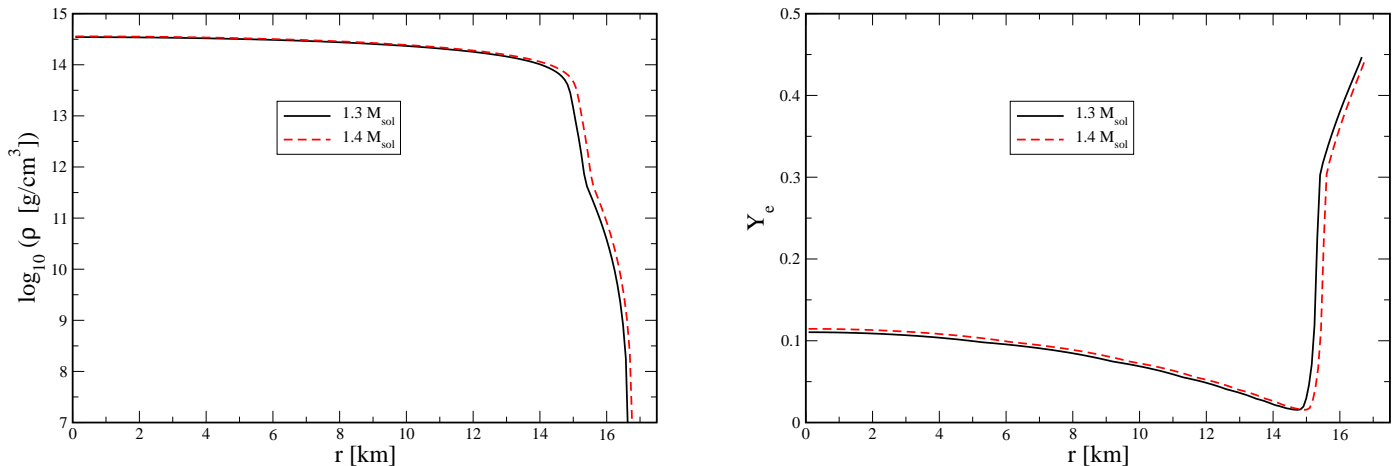


Figure 1. Initial density and Y_e profiles (in hydrostatic and β -equilibrium) of the neutron stars used in this study (1.3 and $1.4 M_{\odot}$, nuclear equation of state of Shen et al. (Shen et al. 1998a)).

events that involve a large variety of different physical processes, see Faber (2009), Duez (2010), Shibata & Taniguchi (2011), Rosswog (2011) and Faber & Rasio (2012) for recent reviews on various aspects of this topic and for a guide to the current literature.

The detection of the gravitational waves (GWs) emitted during the inspiral of ns^2 and nsbh binary mergers are prime targets of ground-based gravitational wave detectors such as LIGO, Virgo and GEO600 (Willke et al. 2006; Acernese et al. 2008; Grote 2008; Smith 2009). In their advanced states, the interferometers target to detect the signals of ns^2 coalescences out to hundreds of megaparsecs, corresponding to redshifts of $z \approx 0.1$. Once detected, the gravitational waves offer the exciting possibility of filling gaps in our understanding of the neutron star equation of state in the high density, low temperature regime that is experimentally hardly accessible.

Compact binaries have for a long time been the prime candidates for the central engines of (short) gamma-ray bursts (GRBs; Eichler et al. (1989); Paczyński (1991); Narayan et al. (1992)) and this hypothesis has survived being confronted with a wealth of observational results in recent years. Several challenges remain, however, and the case is far from being closed (Piran 2005; Nakar 2007; Lee & Ramirez-Ruiz 2007; Gehrels et al. 2009).

They are also promising sources for the heaviest elements in the Universe that are formed via rapid neutron capture (Lattimer & Schramm 1974, 1976; Eichler et al. 1989; Freiburghaus et al. 1999; Rosswog et al. 1999; Roberts et al. 2011; Goriely et al. 2011). The textbook r-process source, core-collapse supernovae, have been found to be seriously challenged in providing the physical conditions (high entropy, low electron fraction together with rapid expansion) that are required to produce the heavy ($A > 90$) r-process elements (Roberts et al. 2010; Fischer et al. 2010; Arcones

& Janka 2011)¹. The main r-process nucleosynthesis contenders are compact binary mergers which release neutron-rich matter in at least three ways. Apart from the matter that is ejected dynamically via gravitational torques, there is an additional contribution due to neutrino-driven winds (Dessart et al. 2009) and from the late-time dissolution of accretion disks (Chen & Beloborodov 2007; Beloborodov 2008; Metzger et al. 2008). While the initial starting point is the same, cold neutron star matter in β -equilibrium, the three channels differ in the amounts of released matter, in their entropies, expansion time scales and electron fractions. Therefore they might possibly produce different nucleosynthetic signatures.

The ejecta are responsible for two types of electromagnetic transients: the decompressed neutron star matter is subject to radioactive decays (Li & Paczyński 1998; Rosswog 2005; Metzger et al. 2010; Roberts et al. 2011) and at some stage the ejecta dissipate their kinetic energy in the ambient medium. The former is expected to produce an optical display not too different from a supernova, but much shorter, sometimes referred to as “macronova”, the latter has been shown to produce detectable, isotropic radio emission that peaks near one gigahertz and persists on a detectable (sub-milliJansky) level for weeks out to a distance of $z \approx 0.1$ (Nakar & Piran 2011). Especially if the true GW detection rates should be near the lower end of the predictions, additional electromagnetic signatures would be crucial to confirm marginal gravitational wave detections and they would therefore enhance the effective detector sensitivities (Kochanek & Piran 1993; Hughes & Holz 2003; Dalal et al. 2006; Arun et al. 2009).

¹ A possible exception may be magnetorotationally driven supernova jets where interestingly low electron fraction values seem to be reachable (Winteler et al. 2012). It remains to be explored, however, how robust this scenario is with respect to the stellar parameters and with respect to its nucleosynthetic yields.

Recently, dynamical collisions between compact objects as they may occur in the core of globular clusters have been studied by several authors (Kocsis et al. 2006; O’Leary et al. 2009; Lee et al. 2010; Kocsis & Levin 2012). Lee et al. (2010) concluded that collisions could produce GRBs at a detectable rate. To demonstrate the viability as GRB engines they performed hydrodynamic simulations of compact object collisions, though without use of detailed microphysics such as a nuclear equation of state or neutrino emission.

The main questions that we want to address in this paper are:

- a) In which ways do the remnants and signatures of dynamical collisions differ from those of binary mergers?
- b) To which extent can their rate be constrained by nucleosynthetic yields?
- c) How different are electromagnetic transients following mergers and collisions?

To address these issues we performed a sizeable set of Newtonian hydrodynamics simulations which include a nuclear equation of state and an opacity-dependent neutrino cooling scheme. These simulations are subsequently explored to predict the electromagnetic signatures of compact binary encounters. Clearly, the investigated systems are relativistic and ultimately General Relativity should be applied. It is, however, not gravity alone that shapes the dynamics and observable signatures of these encounters. Instead, also the remaining fundamental interactions contribute their share: a) the strong interaction via the nuclear equation of state, b) the weak interaction since it determines the neutrino emission rates and thus the evolution of the electron fraction Y_e and c) the electromagnetic interaction which is, for example, responsible for producing radio-flares once ejected material dissipates its kinetic energy in the ambient medium. Given this complexity, we consider Newtonian gravity as a tolerable approximation for the time being. The presented simulations are meant to serve as benchmarks for future simulations that may include general relativity and the relevant microphysics.

We discuss the viability of dynamical collisions as GRB central engines, in particular the properties of remnant disks, their neutrino emission and the prospects for magnetic field amplification. We further calculate the mass and the return time scales of fallback and we present in detail the properties of dynamical ejecta as a basis for subsequent nucleosynthesis calculations. Based on these findings we discuss the question “What is the electromagnetic signature of a ns^2 and a nsbh encounter?”

The paper is structured as follows. In Sec. 2 we briefly summarize the ingredients of our simulations both in terms of physics and numerical methods. In Sec. 3 we describe the main findings. Sec. 3.1 discusses the dynamics and its imprint on gravitational waves, Sec. 3.2 explores the neutrino signal and Sec. 3.3 the differences between merger and collision fallback. In Sec. 3.4 we discuss the properties of the dynamically ejected material such as mass, electron fraction and velocity structure. They all shape the electromagnetic display, which is addressed in Sec. 3.5. Our results are summarized and discussed in Sec. 4.

2 SIMULATIONS

The simulations of this paper make use of the Smooth Particle Hydrodynamics (SPH) method, see Monaghan (2005) and Rosswog (2009) for recent reviews. Our code is an updated version of the one that was used in earlier studies (Rosswog & Davies 2002; Rosswog & Liebendörfer 2003; Rosswog et al. 2003; Rosswog 2005). We solve the following evolution equations for each particle a

$$\frac{d\vec{v}_a}{dt} = - \sum_b m_b \left(\frac{P_a}{\rho_a^2} + \frac{P_b}{\rho_b^2} + \Pi_{ab} \right) \nabla_a W_{ab} + \vec{f}_{a,g} + \vec{f}_{a,\text{GW}} \quad (1)$$

$$\frac{du_a}{dt} = \sum_b m_b \left(\frac{P_a}{\rho_a^2} + \frac{1}{2} \Pi_{ab} \right) \vec{v}_{ab} \cdot \nabla_a W_{ab} - \frac{du_a^\nu}{dt} \quad (2)$$

$$\frac{dY_{e,b}}{dt} = \lambda_{\text{PC}} Y_n - \lambda_{\text{EC}} Y_n, \quad (3)$$

the mass density is calculated by summing up contributions from neighboring particles

$$\rho_a = \sum_b m_b W_{ab}. \quad (4)$$

Here m_b is the (constant) mass of particle b and $W_{ab} = W(|\vec{r}_a - \vec{r}_b|, h_{ab})$ denotes the cubic spline kernel (Monaghan 1985) evaluated with the average smoothing length $h_{ab} = (h_a + h_b)/2$. $\vec{f}_{a,g}$ is the additional acceleration due to self-gravity that we evaluate using a binary tree (Benz et al. 1990) and $\vec{f}_{a,\text{GW}}$ results from gravitational wave back-reaction. The relative particle velocity is denoted as $\vec{v}_{ab} = \vec{v}_a - \vec{v}_b$. To produce entropy in shocks artificial dissipation is included via the tensor Π_{ab} . It has the standard form Monaghan (1992) but particular care has been taken to avoid possible artifacts due to artificial viscosity, this has been outlined in detail in Rosswog et al. (2008). The quantity u_a denotes the specific internal energy of particle a the evolution of which is determined by PdV -work and viscous heating (summation term) and the energy loss to neutrinos, $\frac{du_a^\nu}{dt}$. The quantities

$$\lambda_{\text{PC}} = \frac{R_{\text{PC}}^{\text{eff}}}{\eta_{\text{np}}} \quad \text{and} \quad \lambda_{\text{EC}} = \frac{R_{\text{EC}}^{\text{eff}}}{\eta_{\text{pn}}} \quad (5)$$

are the electron and positron capture rates per neutron/proton. $R_{\text{EC/PC}}^{\text{eff}}$ are the effective neutrino number emission rates and the quantities $\eta_{\text{np}}/\eta_{\text{pn}}$ reduce in the non-degenerate limit to the number densities n_n and n_p (Bruenn 1985), for a more detailed account on the neutrino treatment we refer to the original paper (Rosswog & Liebendörfer 2003). The pressure at a particle b , $P_b(\rho_b, T_b, Y_{e,b})$, is calculated using the Shen et al. equation of state (EOS) (Shen et al. 1998a,b) extended to lower densities as described in Rosswog & Davies (2002).

Compact binary systems are driven towards coalescence via the emission of gravitational waves. The corresponding radiation reaction forces for a slow-motion, weak field source can be calculated as the gradient of a radiation reaction potential which contains the fifth time derivatives of the reduced quadrupole moments (Burke 1971). Simple backreaction prescriptions usually rely on reducing the order of the time derivatives by averaging over several orbital periods. This procedure is well justified during the secular inspiral stages of a compact binary merger, but it has no well-defined meaning in the case of a parabolic encounter. For this reason

we ignore the exerted backreaction for the *collision* cases of this first study, for the merger cases we use a simple point mass description (Davies et al. 1994) for $\tilde{f}_{a,\text{GW}}$. The possible impact of this technical shortcoming will be discussed below.

As a diagnostics of the dynamical evolution we will use below the gravitational wave amplitudes as seen by an observer located along the binary rotation axis. Consistent with the Newtonian treatment of gravity we extract gravitational waves in quadrupole approximation

$$h_+^{\text{TT}} = \frac{1}{d} \frac{G}{c^4} (\ddot{I}^{xx} - \ddot{I}^{yy}) \quad (6)$$

$$h_\times^{\text{TT}} = \frac{2}{d} \frac{G}{c^4} \ddot{I}^{xy}, \quad (7)$$

where I^{ij} is the reduced quadrupole moment tensor evaluated at retarded times,

$$I^{ij} = \sum_b m_b (x_b^i x_b^j - \frac{1}{3} \delta^{ij} r_b^2). \quad (8)$$

The needed time derivatives can be obtained by straight forward differentiation of Eq.(8) so that the amplitudes can be calculated as sums involving particle masses, positions, velocities and forces.

In the presented simulations we restrict our collision study to parabolic orbits. The strength of such an encounter is parametrized by the parameter

$$\beta \equiv \frac{R_1 + R_2}{r_P}, \quad (9)$$

where the R_i are the neutron star/Schwarzschild radii of the involved objects and r_P is the pericenter distance. Thus $\beta = 1$ corresponds to a grazing impact, stronger (weaker) impacts have larger (smaller) values. Since the collision rates are proportional to the pericenter distance r_P , we consider run A with $\beta = 1$ as the most likely ns² collision case. Collisions with pericenter distances $\beta < 1$ can still form tidal capture binaries (Fabian et al. 1975; Lee et al. 2010) which can lead to final collisions after a sequence of pericenter passages. Collisions with $\beta < 1$, however, become computationally increasingly cumbersome due to the discrepancy between orbital and internal dynamical time scales. Therefore we only consider collisions with $\beta \geq 1$. To keep the explored parameter space under control, all investigated nsbh collisions possess a fixed impact strength of $\beta = 1$ and we only vary the black hole mass.

It has long been known that the ns mass distribution possesses a narrow peak near $1.35 M_\odot$ (Thorsett & Chakrabarti 1999). Recent studies find an additional broader peak around $1.5\text{--}1.7 M_\odot$ (Kiziltan et al. 2010; Valentim et al. 2011) for neutron stars with white dwarf companions. There may be an additional low-mass peak near $1.25 M_\odot$ produced by electron capture supernovae (Podsiadlowski et al. 2004; van den Heuvel 2004; Schwab et al. 2010). The mass distributions for neutron stars of different evolutionary paths have recently been discussed in Özel et al. (2012). In our simulations we restrict ourselves conservatively to masses near the $1.33 M_\odot$ peak that the latter authors find for double neutron star systems.

In ns² collision cases we use masses of 1.3 and $1.4 M_\odot$ and explore the dependence on the impact strength parameter β . For nsbh collisions we use a neutron star of $1.3 M_\odot$ and we

investigate the dependence on the black hole mass ($m_{\text{bh}} = 3, 5$ and $10 M_\odot$) while keeping the impact parameter at $\beta = 1$. We consider run H with $m_1 = 1.3 M_\odot$, $m_2 = 1.4 M_\odot$, i.e. $q \approx 0.923$ and negligible spins (Bildsten & Cutler 1992; Kochanek 1992) as the generic merger case and we will use it frequently as a reference point to compare the other cases against. As a somewhat academic case, we explore an initially tidally locked binary neutron star system in run G. In runs I and J we briefly touch upon neutron star black hole mergers where the black hole is treated as a Newtonian point mass with an absorbing boundary at the Schwarzschild radius.

The initial neutron stars are constructed from spherically symmetric, zero-temperature, β -equilibrium profiles, see Fig. 1. The SPH particles are placed in a close packed, hexagonal lattice configuration and they are subsequently relaxed so that they can find their true numerical equilibrium state, see Sect. 3.1 of Rosswog & Price (2007). Some of our simulations have been run up to 0.5 s, more than an order of magnitude longer than existing simulations on this topic.

All performed simulations are summarized in Tab. 1.

3 RESULTS

3.1 Encounter dynamics and gravitational wave emission

To set the stage for later comparisons, we start with a brief description of the “standard” binary merger case, run H. In Fig. 2 we show a 3D rendering of its temperature distribution. We only display matter below the orbital plane so that the temperatures and flow structures inside the central remnant can be easily grasped. About one orbital period after contact two asymmetric spiral arms have formed (panel one and two), which evolve during the next ~ 15 milliseconds into a nearly axisymmetric torus (panel 4). When the stars come into contact a shear interface forms between them. Such Kelvin-Helmholtz unstable interfaces have long been known to emerge in neutron star mergers, see, for example, Ruffert et al. (1996); Rosswog et al. (1999); Rasio & Shapiro (1999). The resulting vortices have also been found to locally amplify pre-existing magnetic fields (Price & Rosswog 2006; Anderson et al. 2008; Obergaulinger et al. 2010) and inside of them the (SPH particle) temperatures can temporarily reach values in excess of 60 MeV. The somewhat academic case of an initially tidally locked binary shows more pronounced tidal tails (due to larger angular momentum), but similar temperatures. Both double neutron star merger cases produce reasonably well-defined massive tori of $0.25 M_\odot$ in the irrotational “standard” case and $0.30 M_\odot$ for tidal locking, see Tab. 2.

The collision cases in contrast can suffer several close encounters before finally merging into a single object and during these passages the neutron stars are efficiently tidally spun up. In the $\beta = 1$ case a single object only forms after the third close encounter, see Fig. 3. In the first, grazing impact the stars’ orbital energy is used to spin up the stars to close to their breakup period, e.g. panel 2, and now they form an eccentric tidal capture binary. The next encounter near $t = 8$ ms is more central and again produces strong

Table 1. Overview over the performed simulations. The impact strength parameter β is defined in Eq. (9).

| Run | m_1 [M_\odot] | m_2 [M_\odot] | β | N_{SPH} [10^6] | t_{end} [ms] | objects/comment |
|-------------------|---------------------|---------------------|---------|-----------------------------|-----------------------|-----------------|
| Collisions | | | | | | |
| A | 1.3 | 1.4 | 1 | 2.7 | 21.2 | ns-ns |
| B | 1.3 | 1.4 | 2 | 8.0 | 9.0 | ns-ns |
| C | 1.3 | 1.4 | 5 | 2.7 | 13.2 | ns-ns |
| D | 1.3 | 3.0 | 1 | 1.3 | 127.5 | ns-bh |
| E | 1.3 | 5.0 | 1 | 1.3 | 143.6 | ns-bh |
| F | 1.3 | 10.0 | 1 | 1.3 | 540.3 | ns-bh |
| Mergers | | | | | | |
| G | 1.3 | 1.4 | n.a. | 2.7 | 20.3 | ns-ns, corot. |
| H | 1.3 | 1.4 | n.a. | 2.7 | 19.1 | ns-ns, no spins |
| I | 1.4 | 5.0 | n.a. | 0.2 | 138.7 | ns-bh, no spins |
| J | 1.4 | 10.0 | n.a. | 0.2 | 139.3 | ns-bh, no spins |

Kelvin-Helmholtz vortices at the interface in which (SPH particle) temperatures locally exceed 80 MeV. The stars separate once more, with the $1.3 M_\odot$ star now transferring mass in a direct impact phase into the primary, see panel 4. The final encounter occurs around $t \approx 12$ ms, again forming a string of Kelvin-Helmholtz vortices (panel 5) and finally shedding mass from the secondary neutron star (panel 6). During the encounter the density never exceeds the initial value ($\approx 3.6 \times 10^{14} \text{ g cm}^{-3}$).

The more central encounters form a single object after two ($\beta = 2$) and just one encounter ($\beta = 5$). In both cases strong shocks form in which the (SPH particle) temperatures reach values in excess of 80 MeV. In such shocks the neutron stars are substantially compressed, to values of $\approx 4.52 \times 10^{14} \text{ g cm}^{-3}$ ($\beta = 2$) and $\approx 5.55 \times 10^{14} \text{ g cm}^{-3}$ ($\beta = 5$). In a superposition of rapid rotation and violent, stellar-radius amplitude oscillations, the central objects produce a multitude of interacting shocks in a string of mass shedding episodes, see Fig. 4. The oscillations are also imprinted on the neutrino signal, see below.

For the neutron star black hole cases we also begin with binary mergers as a reference point. Since they have been explored in detail before (Rosswog et al. 2004; Rosswog 2005; Rosswog 2007b), we restrict ourselves to a brief summary. In the case of a $1.4 M_\odot$ ns and a $5 M_\odot$ bh (run I) the neutron star starts transferring mass into the hole after 1.5 orbital periods. Consistent with our earlier studies this does not lead to the disruption of the neutron star on a dynamical time scale. Instead, self-gravity overcomes tidal forces again and the neutron star enters a long-lived phase of episodic mass transfer during which it transfers mass periodically towards the hole while shedding mass through its outer Lagrange point². This phase continues for as many as 25 orbital revolutions before the neutron star is finally completely disrupted. The remnant at the end of the simulation ($t = 138.7$ ms) consists of a “disk inside a disk” with a mass of $0.16 M_\odot$

for the inner, high density disk ($\rho > 10^{11} \text{ g cm}^{-3}$, $r < 120$ km) and $0.22 M_\odot$ if also the outer disk ($\rho > 10^8 \text{ g cm}^{-3}$, $r < 700$ km) is counted. The dynamics of the $1.4 M_\odot$ (ns) - $10 M_\odot$ (bh) system proceeds in a similar manner, here after 15 orbital revolutions the neutron star is finally disrupted and leaves a $0.20 M_\odot$ disk together with a rapidly expanding one armed spiral structure. All the numerically determined mass transfer durations must be considered as robust lower limits on the true values (Dan et al. 2011).

For the *neutron star black hole collision* cases we only explore the dependence on the black hole mass and keep the impact strength ($\beta = 1$) and neutron star mass ($m_{\text{ns}} = 1.3 M_\odot$) constant. During the first pericenter passage of the $m_{\text{bh}} = 3 M_\odot$ case, run D, the neutron star survives as a tidally spun up (close to break up, $P \approx 0.95$ ms) self-gravitating object, but sheds some of its mass in a tidal tail. When the neutron star passes the black hole after about 5 ms for a second time another tidal tail is produced. Once more, the core of the neutron star survives as a gravitationally bound object. It is only completely disrupted during the third and final pericenter passage at $t \approx 11$ ms. After 127 ms the remnant consists of the bh with $3.98 M_\odot$, surrounded by a massive disk ($\approx 0.15 M_\odot$, see Tab. 2) which is externally fed by three spiral arms. Qualitatively, the $m_{\text{bh}} = 5 M_\odot$ case evolves in a similar manner, see Fig. 5, but now the neutron star core survives even the third passage. At the time when we have to stop the simulation ($t = 144$ ms), the core is, according to its radial velocity, unbound from the black hole. The neutron star core, however, is embedded into the debris gas and might therefore be further braked during its subsequent evolution so that it will possibly fall back towards the bh. In the $m_{\text{bh}} = 10 M_\odot$ case the neutron star is already completely disrupted during the second pericenter passage. Consistent with the findings of Lee et al. (2010), all nsbh encounters have in common that they all leave behind a bh with a massive remnant disk (see Tab. 2) and one tidal tail per close encounter.

The orbital dynamics is imprinted on the gravitational wave (GW) signal, for its calculation see Sec. 2. For the neutron star mergers (run G and H) the gravitational wave amplitudes h_+ (times the distance to the source d as measured in code units of 1.5 km) are shown in Fig. 6, upper left

² Phases of stable mass transfer are not restricted to the case of Newtonian gravity. A stiff equation of state (Rosswog et al. 2004), small mass ratios and large bh spin parameters make systems particularly prone to stable mass transfer, see Shibata & Taniguchi (2011) for a further discussion.

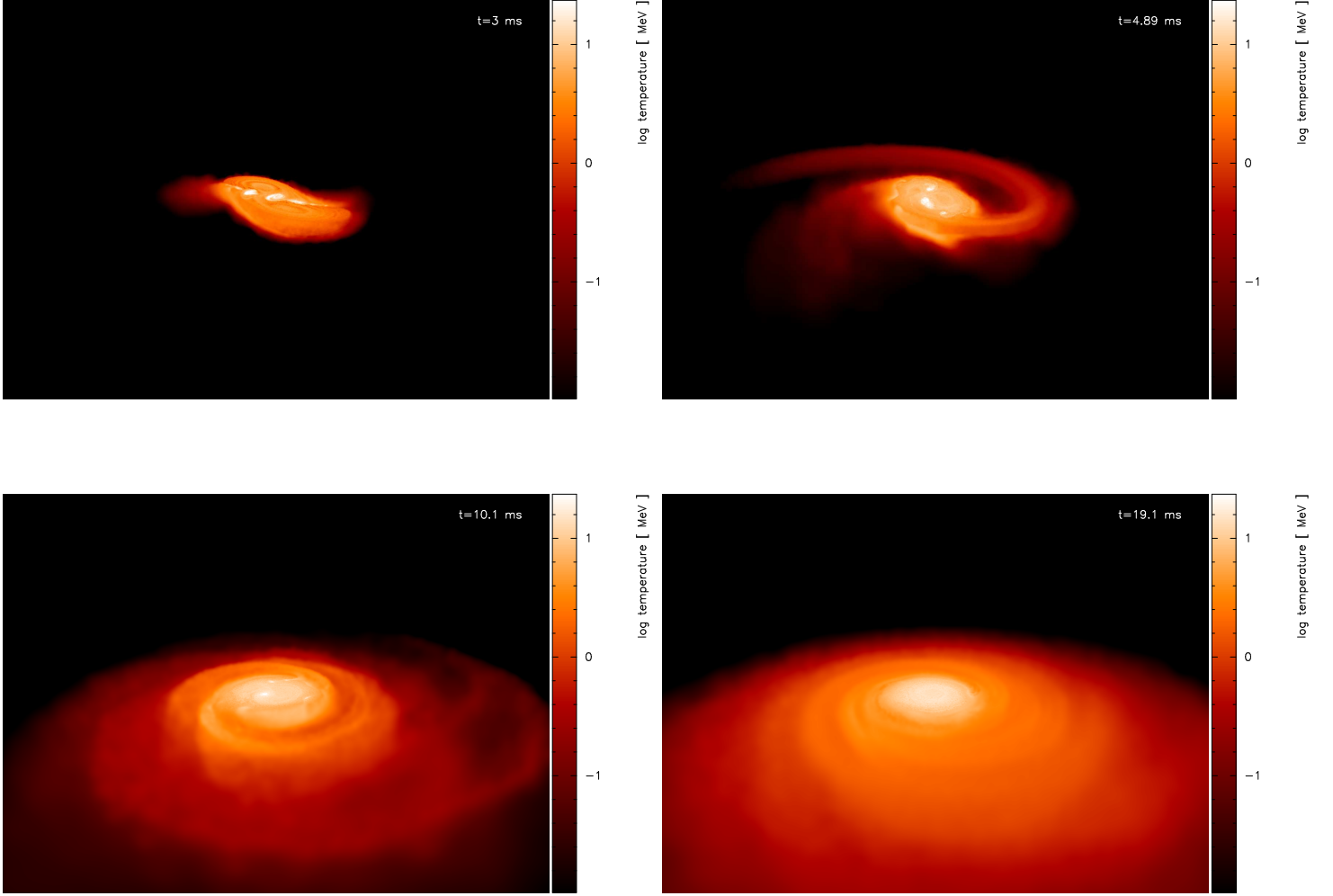


Figure 2. 3D rendering of the temperature distribution in the standard neutron star merger case (1.3 and $1.4 M_{\odot}$, no spin; run H). The upper half of the matter distribution has been “chopped off” to allow for a view into the stars. To enhance the contrast, the upper limit of the colourbar has been fixed to 20 MeV. In the various vortices that emerge due to Kelvin-Helmholtz instabilities peak temperatures in excess of 60 MeV are temporarily reached.

panel. Both cases show the characteristic “chirp”, up to ≈ 3 ms for the non-spinning and up to ≈ 6 ms for the tidally locked case, and the subsequent “ringdown” phase of the non-axisymmetric central object. The amplitudes of the ns^2 collisions are displayed in panel two of Fig. 6. Each close encounter produces a pronounced GW spike, for example in the $\beta = 1$ case, run A, the encounters produce spikes at $t = 2.3, 8.4$ and 12.4 ms. The cases involving black holes show substantially longer activity after the first encounter. In the merger cases, run I and J, the episodic mass transfer is visible for tens of orbits until the neutron star is finally disrupted. The nsbh collision cases are essentially “GW-quiet” (only a small contribution from the close-to-breakup rotation of the neutron star core) when the neutron star is receding from the bh, but produce another GW burst at the next close encounter. For the case with the $5 M_{\odot}$ bh (run E) the longest encountered quiescent phase lasts

as long as ~ 60 ms.

The GW amplitude spikes produced by the close encounters coincide with peaks in the neutrino luminosities, see below. Although the GWs from collisions are comparable in amplitude to those from mergers, the large diversity and the lack of a “standard waveform” will make the detection of collision signals by current and future ground-based gravitational wave detectors extremely challenging.

3.2 Neutrino emission

We discuss the neutrino properties of one example of each encounter class (ns-ns: mergers and collisions; nsbh: mergers and collisions) in some detail, an overview over the properties of all cases is provided in Tab. 3. Again, we use the non-spinning neutron star merger case, run H, as a reference point to gauge the other results. Here, the luminosities

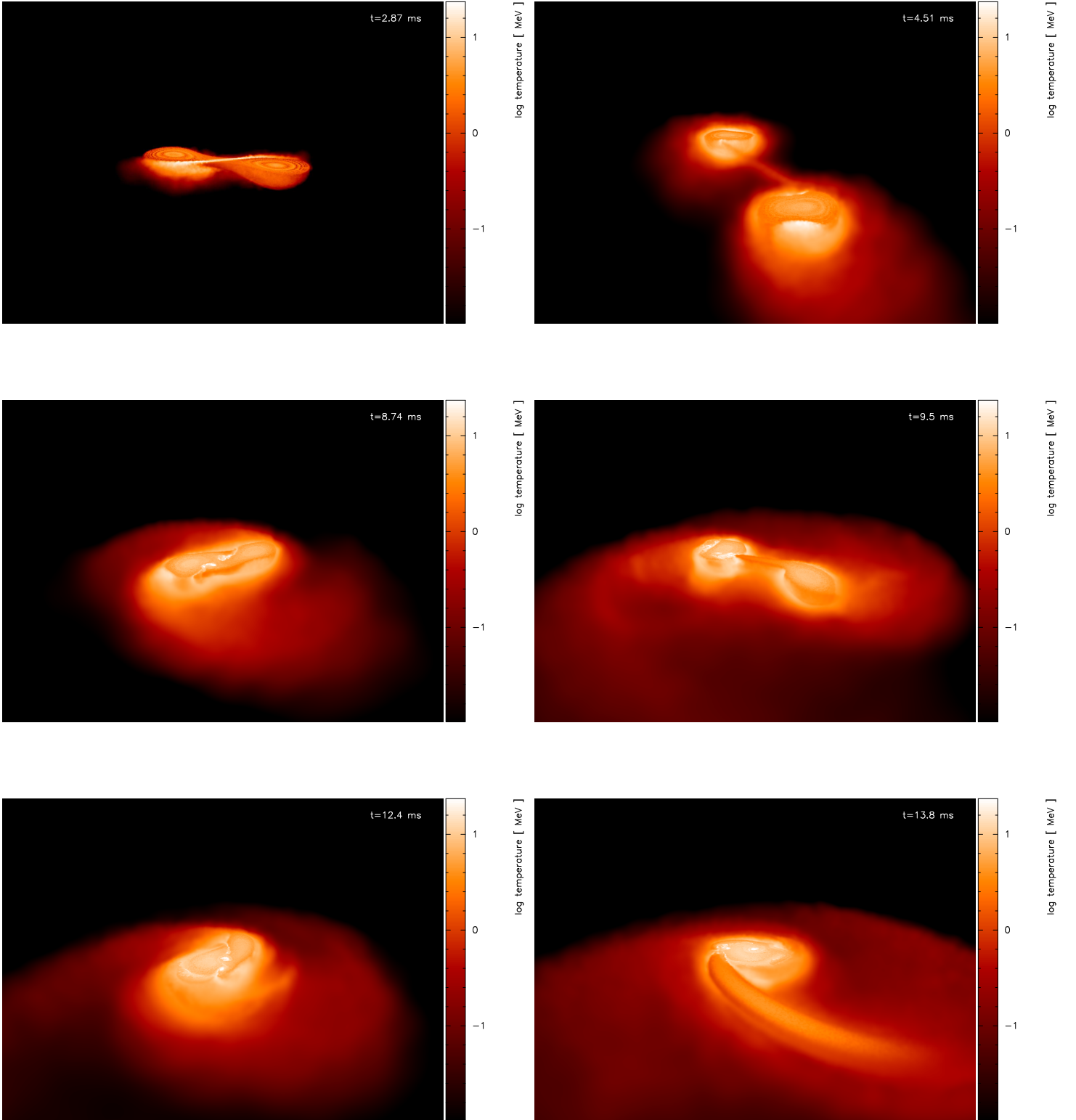


Figure 3. 3D rendering of the temperature distribution during the grazing impact of two neutron stars (1.3 and $1.4 M_{\odot}$, $\beta = 1$; run A). It is only in the third close encounter (panel 5) that finally a single object forms. In each close encounter a slew of Kelvin-Helmholtz vortices forms at the interface between the stars. For display reasons only matter below the orbital plane is shown and the colour bar has been restricted to values below 20 MeV.

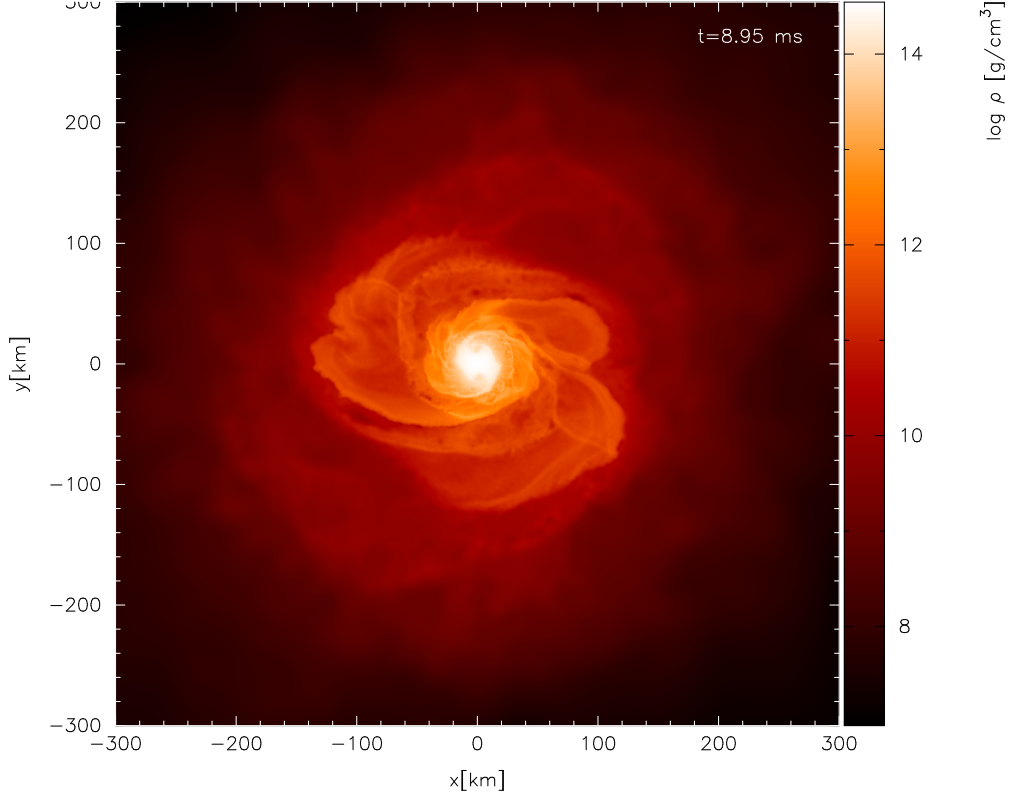


Figure 4. Density cut through the orbital plane at the end of simulation run B (neutron stars with 1.3 and $1.4 M_{\odot}$, $\beta = 2$). The rotating and pulsating central object undergoes a sequence of mass shedding episodes, thereby producing various interacting shocks around the central remnant.

Table 2. Mass distribution: t_{ana} is the time at which we analyze the simulation data, m_{disk} is the resulting disk mass, m_{fb} is the mass in fallback material, m_{esc} is the dynamically ejected mass and E_{kin} the corresponding kinetic energy. Consistent with our approach in Sect. 3.5 we capped the numerical velocities in the calculation of $E_{\text{kin,esc}}$ at $0.75 c$.

| Run | t_{ana} [ms] | m_{disk} [M_{\odot}] | m_{fb} [M_{\odot}] | m_{esc} [M_{\odot}] | E_{kin} [10^{51} erg] | $\langle v_{\text{esc}} \rangle$ [c] | comment |
|-------------------|-----------------------|-----------------------------------|---------------------------------|----------------------------------|-----------------------------------|--------------------------------------|----------------------------------|
| <u>Collisions</u> | | | | | | | |
| A | 21.2 | 0.27 | 0.10 | 0.060 | 1.15 | 0.13 | ns-ns |
| B | 9.0 | 0.40 | 0.10 | 0.009 | 0.97 | 0.22 | ns-ns |
| C | 13.2 | 0.32 | 0.03 | 0.030 | 3.61 | 0.28 | ns-ns |
| D | 127.5 | 0.24 | 0.11 | 0.142 | 5.70 | 0.19 | ns-bh |
| E | 143.6 | 0.14 | 0.04 | 0.172 | 10.68 | 0.24 | ns-bh |
| F | 540.3 | 0.05 | 0.04 | 0.134 | 8.73 | 0.24 | ns-bh |
| <u>Mergers</u> | | | | | | | |
| G | 20.3 | 0.30 | 0.06 | 0.050 | 1.15 | 0.15 | ns-ns, corot. |
| H | 19.1 | 0.25 | 0.04 | 0.014 | 0.23 | 0.12 | ns-ns, no spins |
| I | 138.7 | 0.16/0.22 | 0.04 | 0.024 | 0.61 | 0.15 | “disk in disk”, inner/both disks |
| J | 139.3 | 0.21 | 0.03 | 0.049 | 1.82 | 0.18 | ns-bh, no spins |

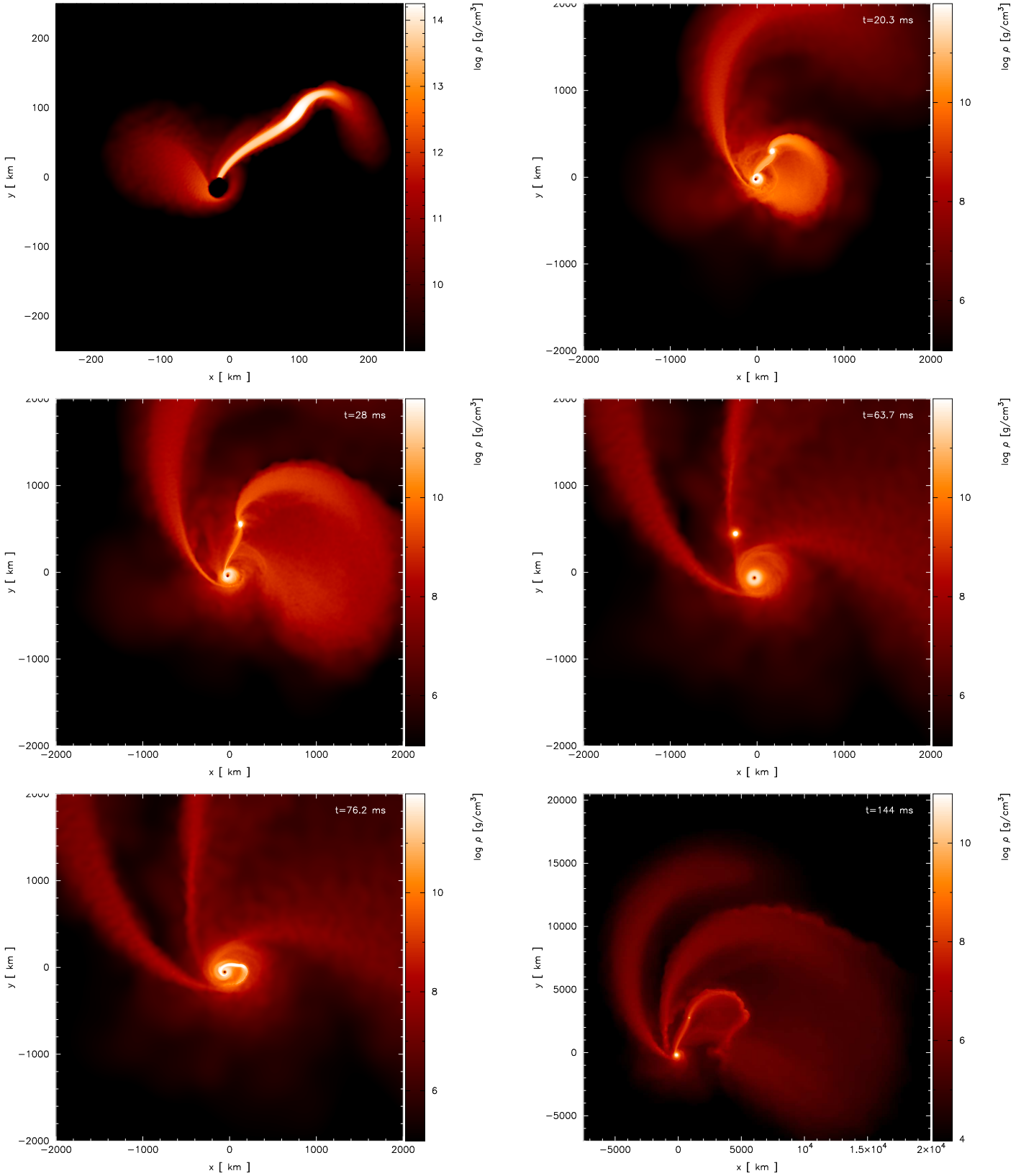


Figure 5. Density cut through orbital plane of run E. Panel one (numbering of the panels is from left to right, from up to down) shows a snapshot just after the first, panel two after the second and panel five just after the third pericenter passage. Each pericenter passage produces a tidal tail. Note that the neutron star core survives even the third pericenter passage. At the end of the simulation it still has a mass of $\sim 0.1 M_{\odot}$ and moves on a close-to-parabolic orbit away from the black hole. Note that the scales are changing between the different snapshots.

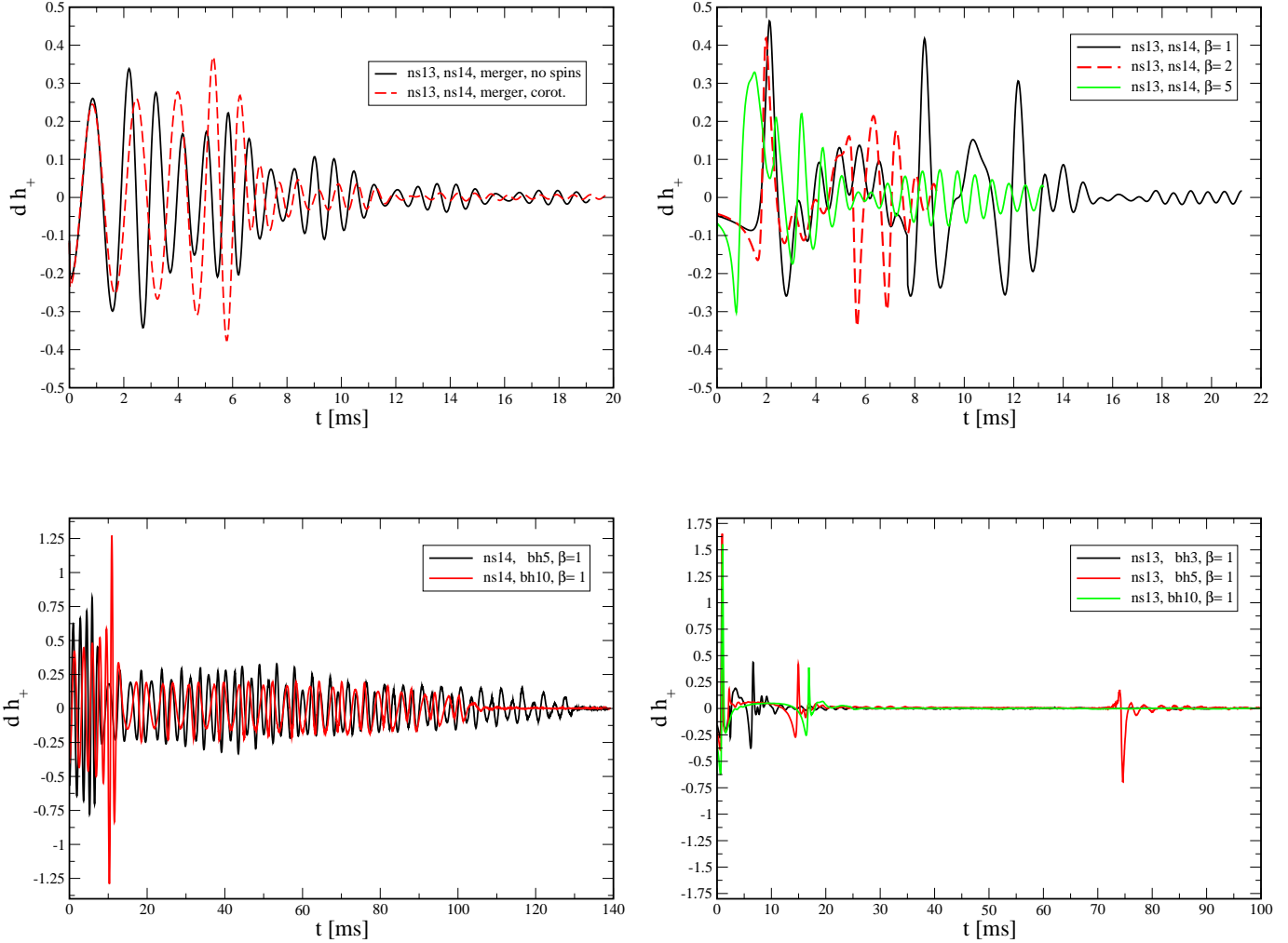


Figure 6. Gravitational wave amplitudes h_+ (times distance to source; code units = 1.5 km). The upper two panels show neutron star neutron star encounters (mergers left, collisions right), the lower two panels show neutron star black hole encounters (mergers left, collisions right).

increase smoothly and peak about 6 ms after contact (at $t \approx 7.7$ ms) with a total of 1.3×10^{53} erg/s, see upper panel of Fig. 7. The tidally locked case, run G, produces similar results, but due to the larger disk mass, see Tab. 2, slightly higher luminosities. Since the debris is extremely neutron-rich, the neutrino luminosities are dominated by electron anti-neutrinos, followed in importance by electron neutrinos and heavy lepton neutrinos (collectively referred to as “ ν_X ”), consistent with earlier findings (Ruffert et al. 1997; Rosswog & Liebendörfer 2003). In a recent 2D neutrino-hydrodynamics calculation starting from the matter distribution that resulted from a 3D simulation (Price & Rosswog 2006) Dessart et al. (2009) found that our leakage scheme underestimates the heavy lepton neutrino emission, since it does not account for the nucleon-nucleon bremsstrahlung process. Therefore our heavy lepton neutrino emission results are robust lower limits on the true luminosities. In all cases apart from run F we find the following hierarchy in

the mean neutrino energies: $\langle E_{\nu_X} \rangle > \langle E_{\bar{\nu}_e} \rangle > \langle E_{\nu_e} \rangle$. The heavy lepton neutrinos are predominantly produced in hot, very dense regions and in the exceptional case, run F, the densities have already dropped substantially below nuclear matter density ($\rho_{\max} < 10^{10} \text{ g cm}^{-3}$) at the end of the simulation when the mean neutrino energies (as given in Tab. 3) are measured.

Even the most gentle ns^2 collision with $\beta = 1$, run A, produces a neutrino luminosity that is approximately three times larger than the standard double neutron star merger case (run H). The merger neutrino lightcurves are rather smooth, the collision cases, in contrast, show a much larger variability with luminosity changes of up to a factor of two on the dynamical time scale of the central object, ≈ 1 ms, see Fig. 7 middle panel. The more central collisions, run B and C, produce neutrino luminosities of about an order of magnitude larger than the reference case, see Tab. 3.

As discussed earlier, we find long-lived, episodic mass trans-

Table 3. Neutrino emission. L_ν refers to the luminosity of all flavors, the average energies, $\langle E \rangle$, are measured in MeV at time t_{ana} , where they are to a very good approximation constant.

| Run | t_{ana} [ms] | $L_{\nu, \text{peak}}$ | $L_\nu(t_{\text{ana}})$ | $\langle E_{\nu_e} \rangle$ | $\langle E_{\bar{\nu}_e} \rangle$ | $\langle E_{\nu_x} \rangle$ | comment |
|-------------------|-----------------------|------------------------|-------------------------|-----------------------------|-----------------------------------|-----------------------------|-----------------|
| <u>Collisions</u> | | | | | | | |
| A | 16.5 | 6.0×10^{53} | 4.3×10^{53} | 10.5 | 15.5 | 23.5 | ns-ns |
| B | 9.0 | 3.0×10^{54} | 1.3×10^{54} | 10.1 | 16.6 | 21.3 | ns-ns |
| C | 13.2 | 4.1×10^{54} | 1.4×10^{54} | 11.0 | 16.1 | 20.8 | ns-ns |
| D | 127.5 | 3.1×10^{53} | 8.1×10^{52} | 7.1 | 10.1 | 21.4 | ns-bh |
| E | 122.9 | 5.3×10^{53} | 5.7×10^{52} | 6.9 | 8.5 | 14.6 | ns-bh |
| F | 540.4 | 1.0×10^{53} | 5.6×10^{51} | 9.0 | 10.6 | 8.9 | ns-bh |
| <u>Mergers</u> | | | | | | | |
| G | 17.5 | 1.8×10^{53} | 1.3×10^{53} | 9.3 | 15.5 | 27.2 | ns-ns, corot. |
| H | 16.0 | 1.3×10^{53} | 9.9×10^{52} | 8.0 | 14.4 | 26.3 | ns-ns, no spins |
| I | 138.7 | 8.9×10^{52} | 5.7×10^{52} | 6.5 | 10.0 | 13.8 | ns-bh, no spins |
| J | 138.7 | 1.0×10^{53} | 6.5×10^{52} | 6.3 | 11.0 | 14.9 | ns-bh, no spins |

fer in the investigated nsbh cases. During this phase the neutrino emission is moderate, but once the neutron star is finally disrupted after dozens of orbital revolutions it reaches peak values of up to 10^{53} erg/s. All investigated nsbh collisions robustly produce hot and massive accretion disks with neutrino peak luminosities of at least 75% of the standard merger case. We display the neutrino luminosities for the case shown in Fig. 5, run E, in the last panel of Fig. 7. All pericenter passages are visible as a peak in the neutrino luminosities. Passages two and three thereby substantially increase the disk mass, the subsequent disk consumption each time produces an enhanced neutrino luminosity. In the case of run E, the enhanced emission due to a pericenter passage is therefore double peaked with a first, short peak resulting from the neutron star remnant impact onto the disk (between panels four and five in Fig. 5), and a second, broader peak driven by the viscous consumption of the re-filled accretion disk. In summary, each pericenter passage produces both a gravitational wave and at least one neutrino emission peak.

3.3 Fallback and external feeding of accretion disks

Swift observations have revealed that both short and long bursts can show late time X-ray flaring activity (Burrows & et al. 2005; Nousek & et al. 2006). Some SWIFT sGRBs are accompanied by a phase of extended X-ray emission that lasts between ~ 10 and 100 s (Norris & Gehrels 2008; Perley et al. 2009) and whose fluence can exceed that of the GRB itself. Such time scales are substantially longer than the dynamical/viscous time scales, i.e. ~ 1 ms/ 0.05 s, that are expected for a merger remnant. In this context, it was pointed out that compact binary mergers possess in addition a much longer time scale due to nearly unbound material that will finally fall back to the central remnant (Rosswog 2007a; Lee & Ramirez-Ruiz 2007; Faber et al. 2006). The mass in the fallback of a merger however is substantially lower than that of the accretion that is supposed to launch the GRB. Therefore it is at least not obvious how fallback would produce extended emission with a larger fluence than the sGRB.

Clearly, the accretion of the fallback material is a rather complicated phenomenon and much of what will finally become visible as electromagnetic radiation will depend on the evolution of the inner remnant disk as it interacts with the fallback material being delivered at super-Eddington rates. It has been argued (Rossi & Begelman 2009) that –rather than being finally swallowed by the likely emerging central black hole– the fallback material could form an extended hot envelope around the remnant once neutrino cooling ceases to be an efficient cooling agent, but the matter is still opaque to photons. After about one week a soft X-ray signal near the Eddington luminosity should become visible.

In addition, while the neutron star debris is initially receding from the central remnant it will be subject to heating from radioactivity (Li & Paczyński 1998; Rosswog 2005; Metzger et al. 2010; Roberts et al. 2011) and it has been proposed that this radioactive energy release might regulate the final fallback rate (Metzger et al. 2010). At the same time, viscous effects drain the disk via accretion onto the central object and the disk expands due to outward angular momentum transport. Winds are expected as a result of viscous heating and/or neutrino heating (Lee et al. 2005; Dessart et al. 2009) which further complicates the situation. At late times, recombinations of nucleons into α -particles are expected to unbind a substantial fraction of the late-time disk (Beloborodov 2008; Lee et al. 2009; Metzger et al. 2009).

Clearly, this interesting, but complicated evolution deserves further detailed studies, but reliable predictions of the electromagnetic display require a reliable knowledge of the properties in the emerging photosphere. The treatment of these effects is beyond the scope of the current work and we restrict ourselves here to a simple semi-analytical model to estimate the time scales on which fallback material is delivered to central object while ignoring for now additional complicating effects such emerging winds.

We assume that for most of its trajectory, the fallback material is reasonably well described as being ballistic. Under this assumption we can calculate quantities like eccentricity, circularization radii etc. as described in detail in Rosswog (2007a) and we can in particular calculate the time, $t_{\text{fb}}(R_{\text{circ}})$, it takes each matter portion to return to

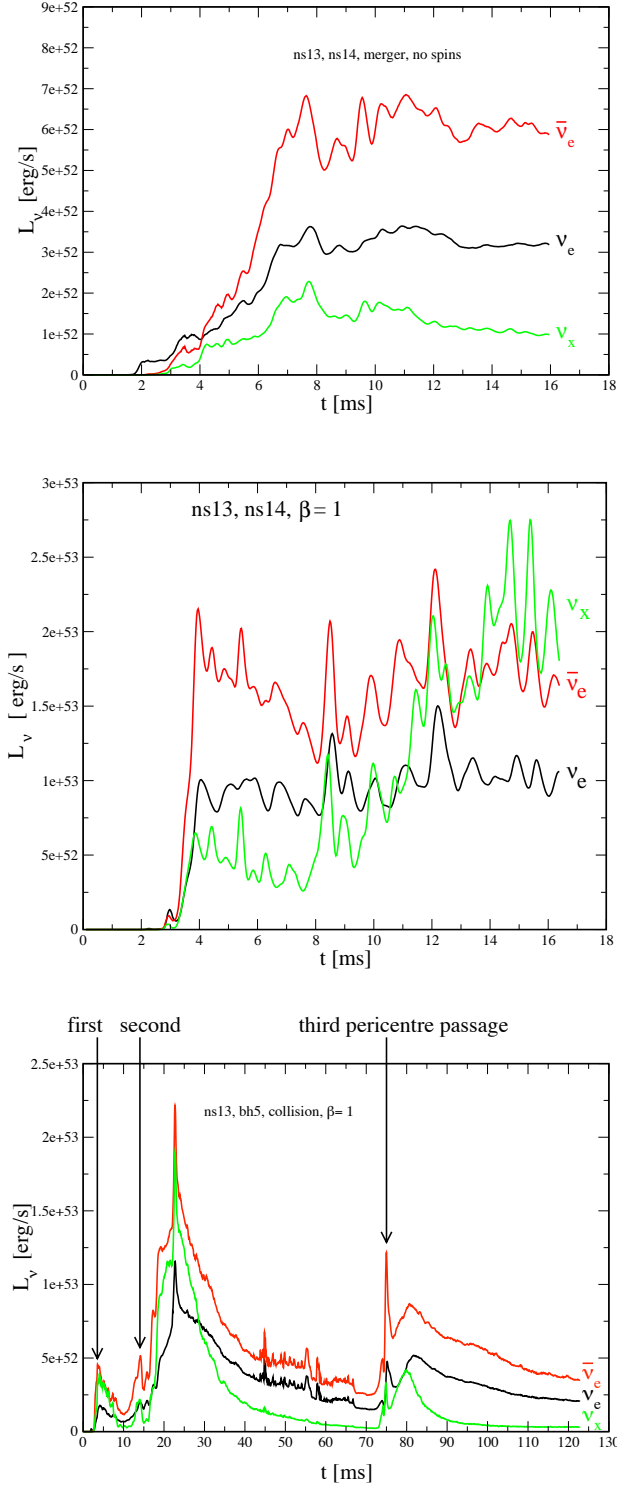


Figure 7. Examples of the emerging neutrino luminosities: the “standard” merger case (run H, upper panel), the ns^2 collision with $\beta = 1$ (run A, middle), and the nsbh collision with $\beta = 1$ and $m_{\text{bh}} = 5 M_{\odot}$ (run E, bottom).

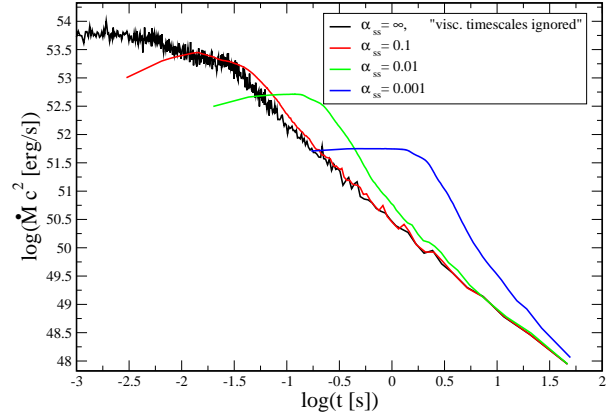


Figure 8. The dependence of the matter energy accretion rate on the Shakura-Sunyaev viscosity parameter α_{ss} is illustrated for the case of a merger between a ns and a $5 M_{\odot}$ bh (run I). Increasing the viscosity time scale (= reducing the parameter α_{ss}) smoothly spreads out the accretion to longer time scales.

its circularization radius, R_{circ} . Under the simplifying assumption that matter quickly settles into a disk, we assume that from this point of time, $t_{\text{fb},a}$, each fluid parcel (SPH particle) a is accreted at a constant rate $\dot{m}_a = m_a/t_{\text{visc},a}$ on the viscous time scale of a thick accretion disk (with $H \sim R$), $t_{\text{visc},a} = (\alpha_{\text{ss}}\Omega_K(R_{\text{circ},a}))^{-1}$, where α_{ss} is the Shakura-Sunyaev viscosity parameter (Shakura & Sunyaev 1973). The total mass accretion rate is then given as a sum over particle contributions

$$\dot{M}(t) = \sum_a \dot{m}_a(t), \quad (10)$$

where

$$\dot{m}_a(t) = \begin{cases} \frac{m_a}{\tau_{\text{visc},a}}, & t_{\text{fb},a} < t \leq t_{\text{fb},a} + \tau_{\text{visc},a} \\ 0, & \text{else} \end{cases} \quad (11)$$

This simple model extends to original one (Rosswog 2007a) by accounting also for the viscous dissipation time scale. Admittedly, this model is very simple and the complicated but important topic fallback accretion in the aftermath of a compact binary merger deserves more efforts in future work.

We illustrate the effect of the viscosity parameter α_{ss} in Fig. 8 for the case of a merger between a ns and a $5 M_{\odot}$ bh (run I). We show the resulting curves $\dot{M}c^2(t)$ for cases where either viscous time scales are ignored (i.e. $\alpha_{\text{ss}} = \infty$) or varied in a plausible range ($\alpha_{\text{ss}} = 0.1, 0.01$ and 0.001).

In Fig. 9 we show the values of $\dot{M}c^2$ from fallback material as predicted from our model. For all shown curves a value of $\alpha_{\text{ss}} = 0.01$ was adopted which is realistic, but maybe slightly on the low side. In our standard merger case, run H, the fallback luminosity peaks around 0.1 s with $\sim 3 \times 10^{52}$ erg/s. The somewhat academic corotating case, run G, shows a similar peak fallback rate which is nearly constant for the first ~ 0.15 s. The $\beta = 1$ ns^2 collision case, run A, produces a roughly constant fallback rate until 0.15 s, before it enters the $5/3$ -powerlaw phase that is expected for $dM/de \approx \text{const}$ (Rees 1988; Phinney 1989). During this

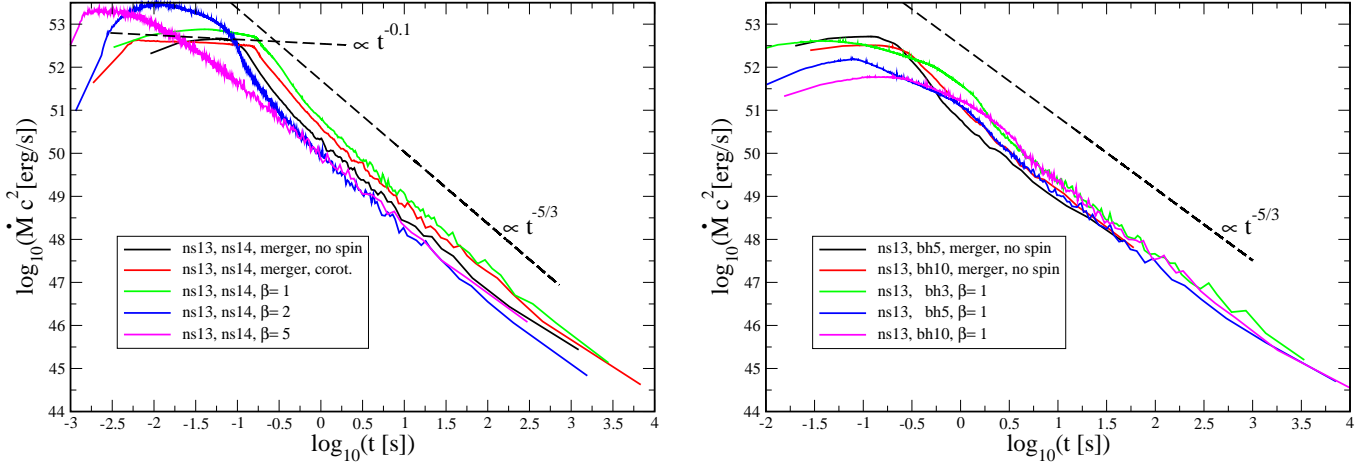


Figure 9. $\dot{M} c^2$ from fallback material as predicted from the simple model (ballistic fallback + disk accretion) described in the main text. Left: neutron star - neutron star cases, right: neutron star - black hole cases. In each panel both merger and collision cases are shown. For comparison we also show the power law for “standard” fallback (Rees 1988; Phinney 1989) that assumes a constant mass per energy, $dm/de = \text{const}$, and results in a time dependence $\propto t^{-5/3}$. For the figures a viscosity value of $\alpha_{\text{SS}} = 0.01$ has been adopted, see text for details.

phase the fallback luminosity is about a factor of four larger than in the standard neutron star merger case. The other ns^2 collision cases peak earlier and their fallback rates are lower than for canonical ns^2 mergers. The early phases of the fallback curves should generally be interpreted with a grain of salt since they are sensitive to the exact location of the disk radius and the assumption of ballistic motion is not necessarily well justified. At later times ($t > 0.2$ s) all cases are fairly well described by the $\dot{M} \propto t^{-5/3}$ powerlaw which is shown in the figure as a dashed line.

The nsbh cases are shown in the right panel. The mergers, run I and J, are qualitatively similar to the ns^2 merger cases, after a “plateau phase” up to ~ 0.3 s, the fallback luminosity drops off compatible with $\dot{M} \propto t^{-5/3}$ (the lack of late time data points for nsbh mergers is due to the substantially lower numerical resolution for these cases). The nsbh collisions show less clear initial plateau phases and only settle into the $5/3$ -powerlaw phase after a few seconds.

The collision cases yield typically about a factor of two more fallback material than the mergers, see Tab. 2. This mass is located in tidal tails (one per pericenter passage) which can be considered as external mass reservoirs that keep replenishing the central accretion disks at their fallback rates. With an available energy of $\sim 2 \times 10^{52} \text{ erg}$ ($\epsilon/0.1$) ($m_{\text{fb}}/0.1 M_{\odot}$) the fallback material is in principle able to produce energetic post-merger activity and, as evident from Fig. 9, the fallback time scales are orders of magnitude longer than the dynamical time scales. But as discussed above, the real situation is possibly too complicated to be adequately captured by this simple fallback + disk model. Therefore it remains an open question whether fallback is the trigger of the late activity that is observed in some sGRBs or not.

3.4 Ejecta

All investigated cases dynamically eject a substantial amount of neutron-rich material, see Tab. 2³. These dynamical ejecta are complemented further by neutrino-driven winds (Dessart et al. 2009) and late-time evaporations of the accretion disks (Beloborodov 2008; Lee et al. 2009; Metzger et al. 2009). The amount of ejecta that we find in the presented simulations is very robust with respect to changing the numerical resolution, it is essentially unchanged even if we reduce the particle number by an order of magnitude. The amount of dynamical ejecta may change, however, with a different treatment of gravitational wave backreaction (reduction), general relativity (probably reduction) or a different nuclear equation of state (depending on EOS stiffness either reduction or enhancement). In earlier work (Rosswog et al. 2000) we had seen the tendency of stiff nuclear equations of state to eject more material than softer ones. The recent discovery of a neutron star close to $2.0 M_{\odot}$ (Demorest et al. 2010) suggests that the true neutron star EOS is indeed very stiff, therefore we consider the Shen et al. EOS as a good choice.

The amount of dynamically ejected material is summarized in Tab. 2. The most likely case, run H, ejects 1.4% of a solar mass with a kinetic energy of $\sim 2 \times 10^{52} \text{ erg}$, the corotating neutron star merger case ejects three times as much mass. The collision cases eject substantially more, about four times as much for the most likely ns^2 collision, run A, and up to 10 times as much for nsbh collision, run E. The kinetic energies in the ejecta can reach up to 10^{52} erg (run E).

The ejected material is extremely neutron-rich and originally resides in the crust and the outer core of the neu-

³ An overview over the ejecta masses for more than 30 different cases can be found in Rosswog (2012).

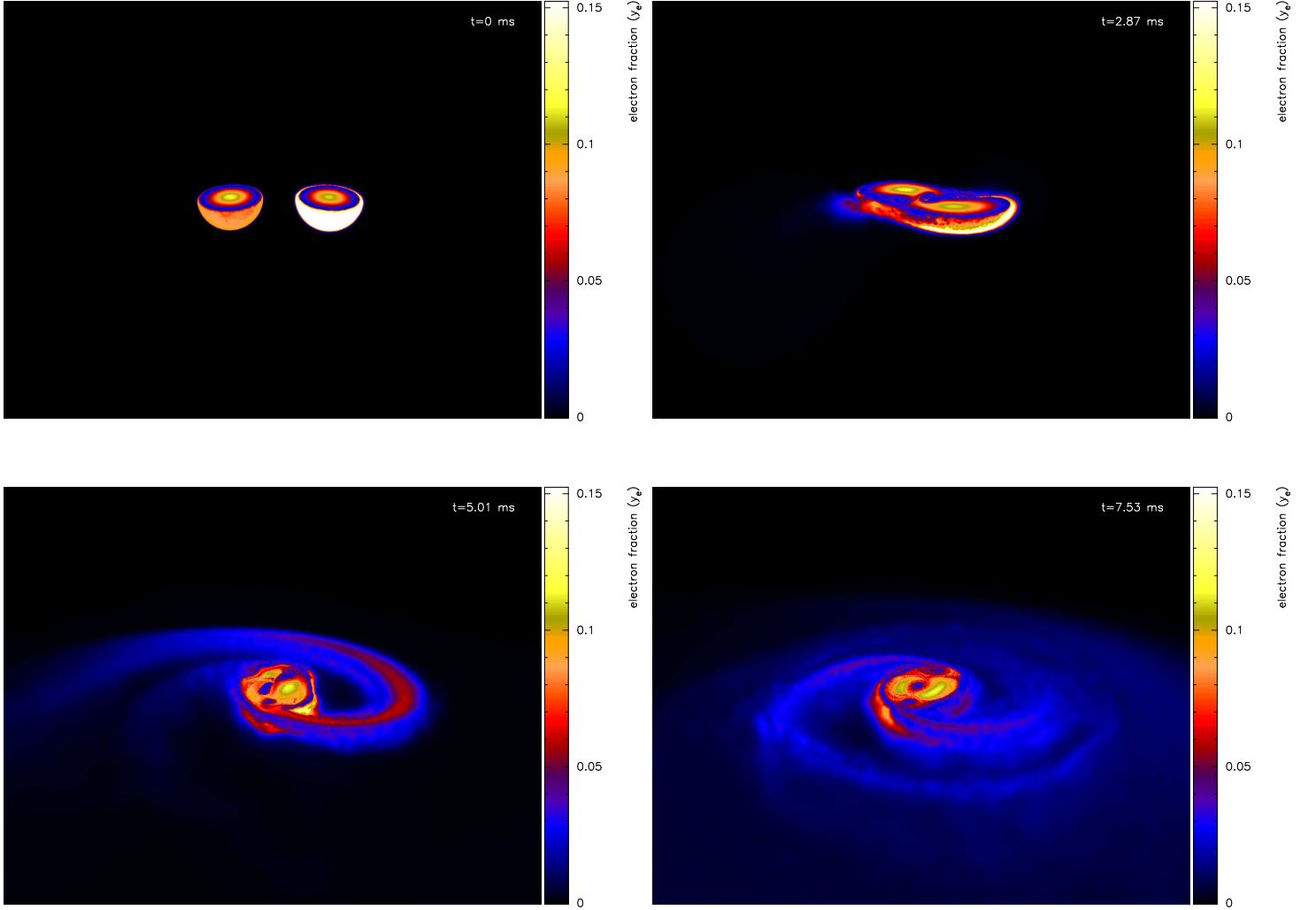


Figure 10. 3D rendering of the Y_e distribution for the generic neutron star merger case ($1.3 M_\odot$, $1.4 M_\odot$, no spins; run H). Only matter below the orbital plane is shown. The bulk of the dynamically ejected matter has Y_e -values as low as ~ 0.03 .

tron star. We display a 3D rendering of the Y_e distribution for our standard neutron star merger case in Fig. 10 (values are shown at a given artificial optical depth, see Price (2007)). The fractional Y_e distribution within the ejecta of the different cases is displayed in Fig. 11. Both neutron star merger cases, runs G and H, upper left panel, eject material with a pronounced peak near $Y_e \approx 0.03$ with (marginally resolved) higher Y_e -contributions from the neutron star crust, see Fig. 1. For the most likely ns^2 collision, run A, the Y_e distribution looks similar (upper left panel). The more extreme –and less likely– more central collision cases ($\beta = 2$ and 5) produce strong shocks with very large temperatures ($T_{\text{peak}} \approx 80$ MeV). In these cases positron captures substantially increase the electron fraction. In both these cases the Y_e distribution has a broad peak near $Y_e \sim 0.2$ (see upper right panel).

The nsbh cases show a similar tendency: where the ejecta are predominantly due to tidal torques they still possess their

original, very low Y_e . If, in contrast, they suffered strong heating in shocks, the Y_e distribution is shifted to larger Y_e values. The nsbh cases experience a different dynamical evolution. In the long episodic mass transfer phase, see Fig. 6, they are continuously tidally heated. In the later stages of mass transfer a disk starts to emerge and there is a continuous hydrodynamic interaction between this growing disk and the ns remnant core. Due to this heating history the Y_e distribution is different: it still shows a peak near $Y_e = 0.03$ but also extends smoothly to values of ~ 0.4 . The collision cases also show somewhat increased Y_e values (~ 0.1) that are due to the various heating phases in the different pericenter passages.

The distribution of asymptotic velocities within the dynamic ejecta is shown in Fig. 12. The distributions in ns^2 merger cases (upper left panel) show peak values around $0.15 c$ and

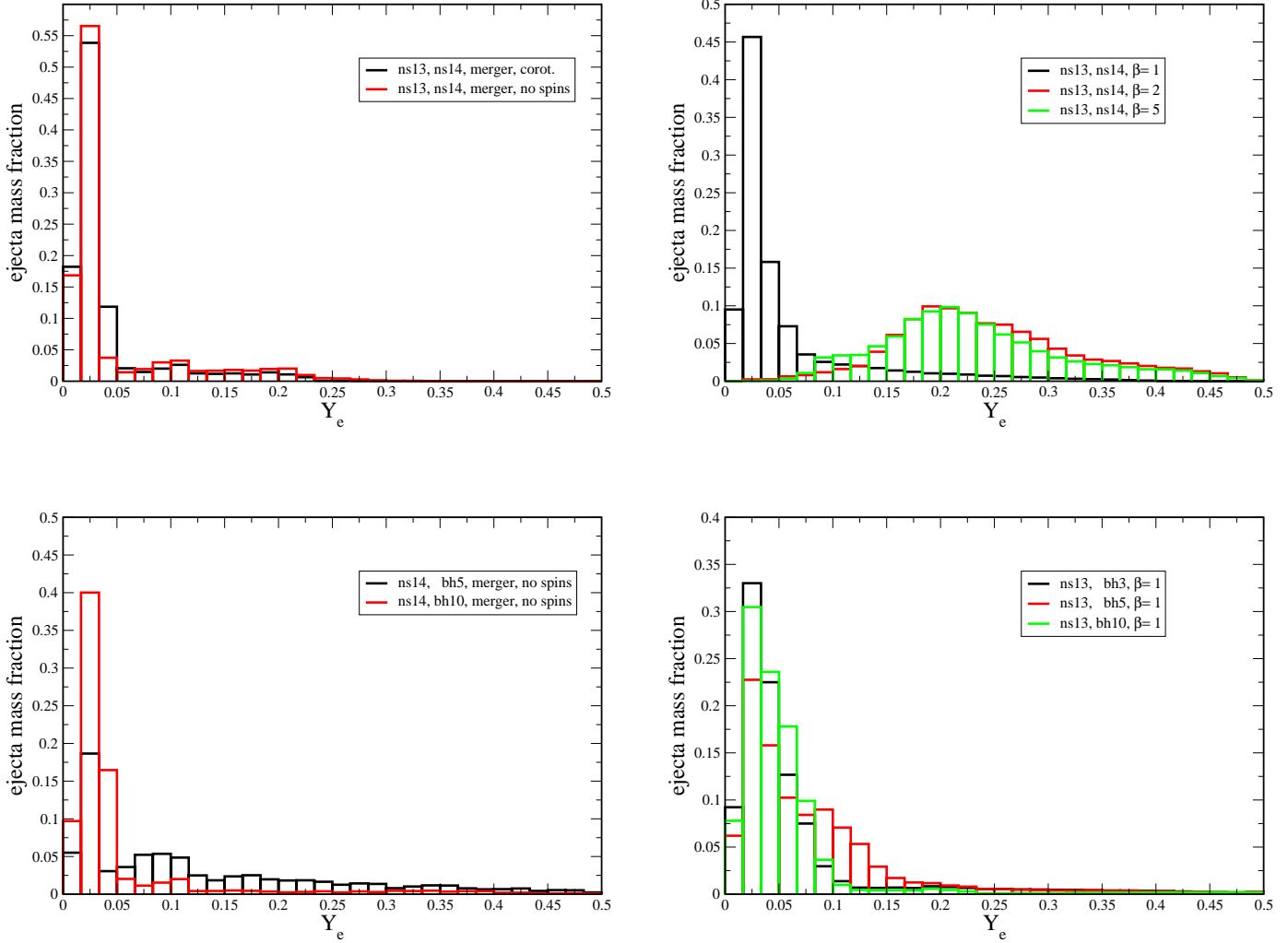


Figure 11. Y_e distribution in the dynamical ejecta binned by mass. The upper row shows double neutron star encounters (mergers left, collisions right), the lower row shows neutron star black hole encounters (mergers left, collisions right).

hardly any material faster than $\sim 0.4 c^4$. The nsbh merger cases show very similar velocity distributions. The collision cases, in contrast, show a much broader distribution of velocities with small mass fractions reaching beyond $0.7 c$, see the right column of Fig. 12. The bulk of ejecta in the grazing ns^2 collision has velocities similar to the merger cases ($\sim 0.15 c$), but smaller amounts of matter can reach substantially higher velocities. The more central collisions show high velocity tails reaching to close to the speed of light. Such close-to- c velocities in the central collision cases ($\beta = 2$ and 5) are likely an artifact of our essentially Newtonian simulations. The nsbh collisions show a very homogeneous behavior with the bulk of matter reaching about $0.3 c$ and

peak velocities out to $0.8 c$. The impact of these properties on the electromagnetic signal is further discussed in Sec. 3.5.

3.5 Electromagnetic emission

3.5.1 Radio remnants from ejecta-ISM interactions

At large radii the sub and mildly relativistic outflow from mergers/collisions is decelerated by the external medium, driving a fast shock into it. Shocks with similar velocities are seen in the late phases of GRBs and in early phases of some supernovae, and are known to produce a bright radio emission. This radio emission is explained by the large fraction of the internal energy behind the shock, $\sim 10\%$, that is channeled into accelerated electrons and a similar amount of energy that goes into magnetic fields. In Nakar & Piran (2011) and in Paper II (Piran et al. 2012) we describe the calculation of the radio emission that follows compact bi-

⁴ We chose the lower limit of the ordinate depending on the numerical resolution. Since the nsbh merger cases have a lower resolution this value differs from the nsns cases.

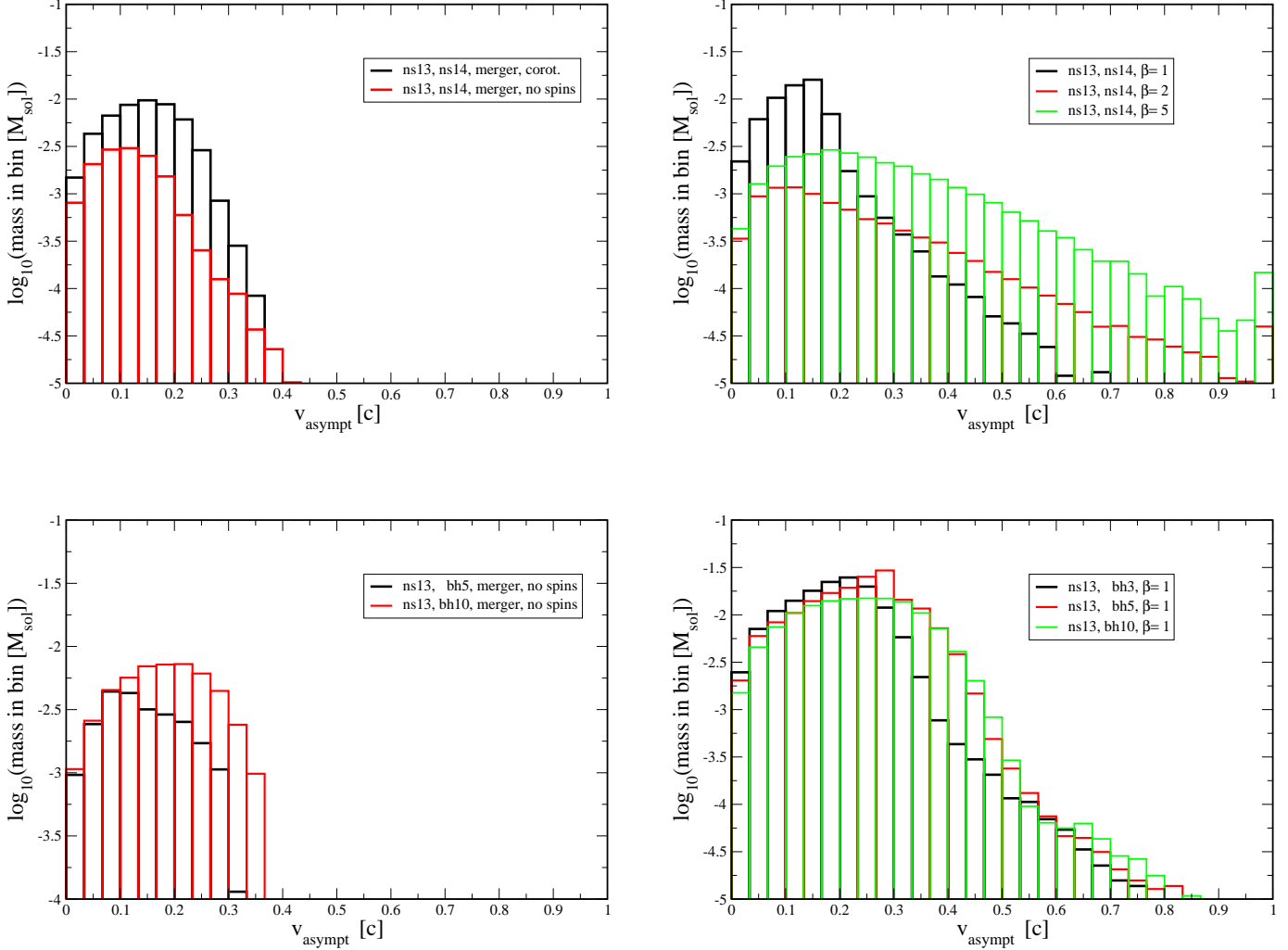


Figure 12. Distribution of the asymptotic velocity within the dynamical ejecta. Upper row ns^2 encounters, mergers left, collisions right. Lower row, nsbh encounters, mergers left, collisions right.

nary mergers. Here we use the same method to compare the radio remnants of mergers and collisions.

In Figs. 13 and 14 we present the radio signal that results from the dynamical ejecta being slowed down by the external medium. The calculation is based on the velocity profiles presented in Fig. 12 and it approximates the interaction as a spherical blast wave in an ambient medium with a constant density, n . Behind the shock constant fractions of the internal energy, $\epsilon_e = 0.1$ and $\epsilon_B = 0.1$, are deposited in relativistic electrons and in magnetic field, where the electrons are accelerated to a power-law with an index $p = 2.5$. The lightcurves are calculated following the procedure described in Paper II (Piran et al. 2012). Since the simulations are Newtonian we do not trust velocities that are close to the speed of light and we therefore conservatively restrict the simulation velocities to a maximum of $0.75\,c$ when using them to calculate the radio emission. Note that the simulations presented here do not include all possible

sources of outflows from such events, and especially sources of mildly relativistic and relativistic ejecta (e.g., various outflow sources from near the event horizon of the accreting black hole, such as Blandford-Znajek (Blandford & Znajek 1977)) are not accounted for. Thus, the true remnants may be brighter than our prediction, especially on short time scales (weeks-months) where the dissipation of the energy in the fastest moving ejecta is most efficient.

The radio lightcurves of ns^2 and nsbh mergers/collisions, see Figs. 13 and 14, are calculated at two frequencies, 1.4 GHz and 150 MHz, and for two values of external densities $n = 1\,\text{cm}^{-3}$ and $n = 0.1\,\text{cm}^{-3}$. The flux normalization is for events at a distance of $10^{27}\,\text{cm}$, roughly at the detection horizon for ns^2 mergers by advanced LIGO and Virgo. The main difference between collisions and mergers is that collisions produce brighter radio remnants that rise faster. Among the collisions the peak flux increases with the penetration factor β . In general the flux from collision remnants

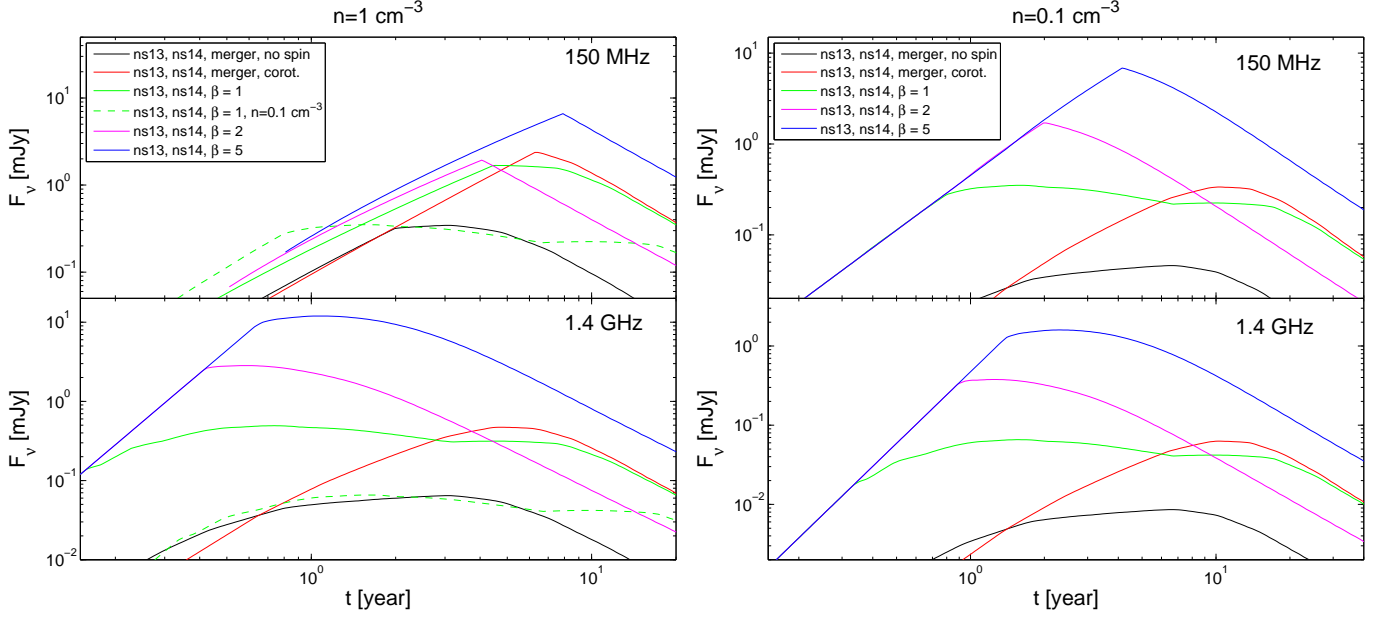


Figure 13. Radio lightcurves of ns^2 mergers and collisions at 150 MHz and 1.4 GHz for two different densities of the external medium (1 cm^{-3} , left and 0.1 cm^{-3} , right). The microphysics parameters are $\epsilon_e = \epsilon_B = 0.1$ and $p = 2.5$, the flux normalization is for events at a distance of 10^{27} cm , roughly the detection horizon for advanced LIGO and VIRGO.

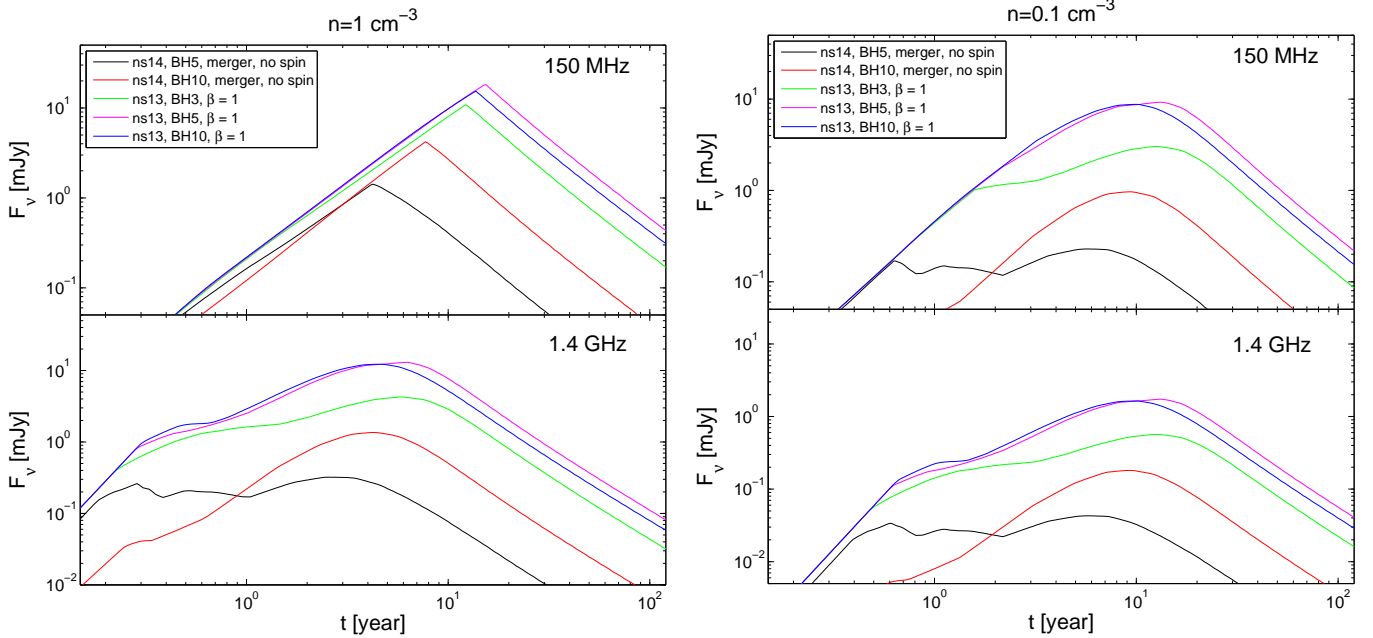


Figure 14. Same as Fig. 13, but for the encounters involving a black hole.

rises fast, within less than a year⁵, and remains bright (or even continues to rise, but more slowly) for several years for ns^2 collisions and for decades in the nsbh collision case. Merger remnants, in contrast, are fainter and they rise over

⁵ The rise time is set in this case by the artificial cut-off ($0.75 c$) that we took in the outflow velocity. A significant outflow with higher velocity results in a shorter rise time.

time scales ranging from a year to a decade and remain bright for a decade or more. The reason for these differences is that collisions are producing more energetic and faster outflows. The larger energy and the faster ejecta increase the remnants' brightness while the faster ejecta are the dominant factor in the shorter rise time, see the detailed discussion in Paper II (Piran et al. 2012) of the effects of the outflow's energy and velocity on the radio signal. Interestingly, a lower external density reduces the flux and slows its

evolution, as long as the observed frequency is above the synchrotron self-absorption at all time. This is the case at 1.4 GHz and therefore, observing at this frequency alone, one cannot distinguish between a ns^2 merger at $n = 1 \text{ cm}^{-3}$ and a collision (with $\beta = 1$) that takes place within a medium of density $n = 0.1 \text{ cm}^{-3}$ (see Fig. 13). The key for removing the degeneracy is to observe the remnant also at 150 MHz, where the effect of the external density on the self-absorption frequency leaves its mark on the lightcurve and makes the two scenarios (merger in dense environment vs. collision in sparse environment) distinguishable.

The major uncertainty concerning the detectability of collisions (the detectability of mergers is discussed in Paper II (Piran et al. 2012)) is due to the external density in globular cluster cores. While globular clusters usually reside in very low density environments, the gas in their cores is expected to be dominated by the mass loss from post main sequence cluster members. The only globular cluster where gas is clearly detected is 47 Tuc, where the density of ionized gas is of order 0.1 cm^{-3} (Freire et al. 2001). This density corresponds to a total mass of $0.1 M_\odot$ in the cluster core. van Loon et al. (2006) reports on a tentative detection of $0.3 M_\odot$ of neutral hydrogen in M15 and possible detections of similar amount of neutral hydrogen in two other clusters (and upper limits of $\sim M_\odot$ in two other). Therefore, it is realistic to expect a circum collision density of 0.1 cm^{-3} , or even larger. nsbh cases are expected to dominate the radio remnant population from collisions, since their volumetric rate is higher (Lee et al. 2010) and they are about ten times brighter. Since these remnants remain bright for decades the best opportunity to identify a remnant is to catch it during its fast rise phase, which takes about a year. Assuming the upper limit for nsbh collisions (6×10^{-6} per Milky way galaxy per year, see below) and taking a detection distance of 1 Gpc (as expected for a sub-mJy survey at 1.4 GHz) the number of remnants which are younger than 1 year, over the whole sky, is < 200 .

3.5.2 Transients from radioactive decays, “macronovae”

As discussed in the previous section, the ejected material is extremely neutron-rich and rapidly expanding. Under such conditions rapid neutron capture is hard to avoid (Hoffman et al. 1996; Freiburghaus et al. 1999; Roberts et al. 2011). The r-process itself occurs on a very short time scale, but the freshly synthesized elements subsequently undergo nuclear fission, alpha- and beta-decay which occur on much longer time scales.

The supernova-like emission powered by this radioactive decay of this expanding material was first suggested by Li & Paczyński (1998) and discussed later by Kulkarni (2005) and Metzger et al. (2010). Here we use the ejecta velocity profile provided by our simulations to calculate the observed light curve following the formalism of Piran et al. (2012) - paper II.

The resulting macronova lightcurves are shown in Fig. 15 for both ns^2 (left) and nsbh encounters (right). The canonical merger case (left, black) peaks after 0.4 days with $\sim 5 \times 10^{41}$ erg/s. The collision cases show a spread in peak times from 0.1 to 1 days and peak luminosities up to 10^{42} erg/s. The macronova resulting from the merger of the $1.4 M_\odot$ ns with a $5 M_\odot$ bh (right, black) is similar to the canonical ns^2 merger

case, the $10 M_\odot$ nsbh merger peaks at about 0.8 days with 10^{42} erg/s. The nsbh collision cases all peak beyond 1 day with $\sim 2 \times 10^{42}$ erg/s.

4 SUMMARY AND DISCUSSION

Dynamical collisions between two neutron stars and a neutron star and a stellar mass black hole are naturally expected in stellar systems with large number densities such as globular clusters. A recent study (Lee et al. 2010) found that dynamical collisions between two neutron stars and a neutron star and a stellar mass black hole occurs more frequently than previously estimated and that such collisions could contribute to the observed sGRB rate. In a large set of simulations we have explored the multi-messenger signatures that are produced by both dynamical collisions and the more conventional gravitational wave driven compact binary mergers. These simulations use Newtonian gravity, but benefit from the use of a nuclear equation of state, a multi-flavour neutrino treatment and a numerical resolution (up to 10^7 SPH particles) that exceeds existing studies by far. Nevertheless, this study will need to be updated once relativistic simulations with microphysics become available.

Dynamics

Generally, collisions show a larger variety in all of their properties than binary mergers, mainly due to the lack of strong constraints on their mass ratio and the impact parameter. Typical velocity dispersions in globular clusters are orders of magnitude smaller than the velocities the compact objects reach due to their mutual gravitational attraction, therefore initially parabolic orbits are good approximations. A compact binary system is already strongly bound at the onset of the dynamical merger phase, collisions, in contrast, possess a total orbital energy close to zero. To finally form a single remnant they have to get rid of energy and angular momentum by gravitational wave emission and mass shedding episodes. Colliding systems therefore undergo several close encounters before they can finally merge into a single central object surrounded by debris. Each close encounter launches a tidal tail and the neutron star(s) is/are spun up to rotation frequencies close to breakup. The final remnant is then, like in the merger case, a supermassive neutron star/black hole surrounded by a disk, but the disk is externally fed by tidal tails (one per close encounter). A good fraction of the mass is still bound to the central remnant and will fall back on times scales substantially exceeding those of the central engine.

GRB engines

We find that collisions are at least as promising as GRB engines as gravitational wave driven binary mergers. For example, ns^2 collisions naturally produce Kelvin-Helmholtz-unstable shear layers in each close encounter, see Fig. 16, which have been found in previous to amplify initial neutron star magnetic fields (Price & Rosswog 2006; Anderson et al. 2008; Obergaulinger et al. 2010) and they robustly form massive accretion disks between ~ 0.05 to $\sim 0.4 M_\odot$. Their neutrino luminosities are at least comparable to the standard neutron star merger case, $\sim 10^{53}$ erg/s, in central

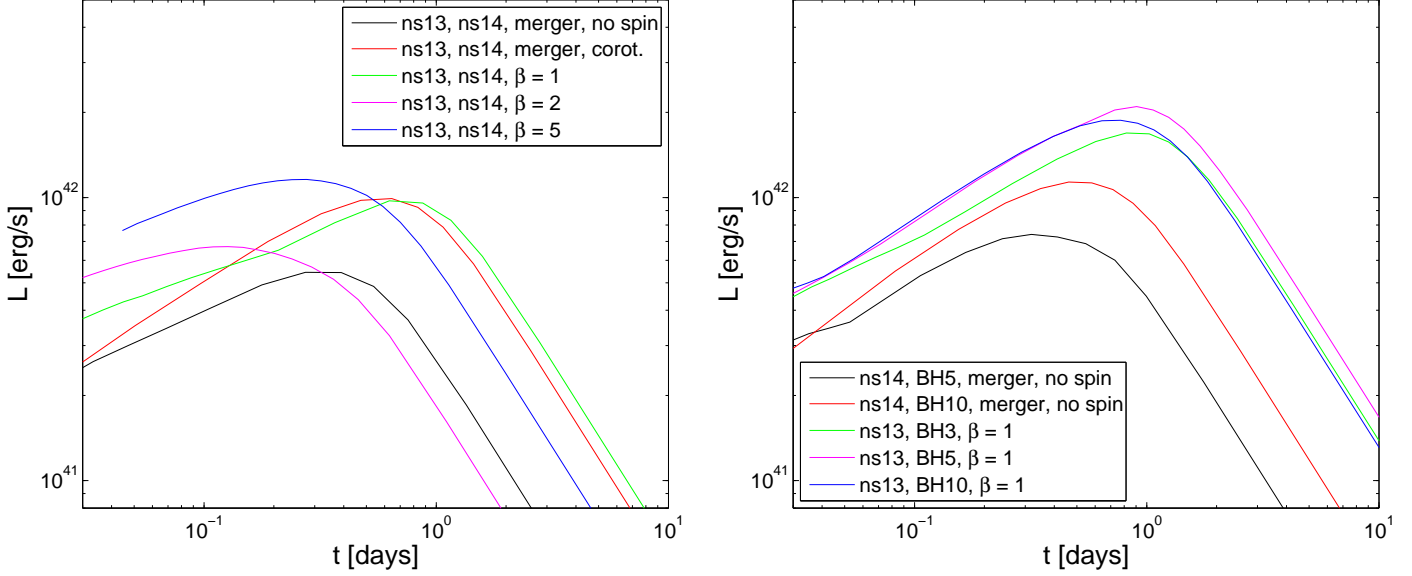


Figure 15. Radioactive decays within the dynamical ejecta produce transient events (“macronovae”) in the optical-UV spectral range that share several properties with supernovae, but evolve on substantially shorter time scales. The lightcurves for ns^2 encounters (mergers and collisions) are shown in the left panel, those of nsbh encounters in the right. See main text for details.

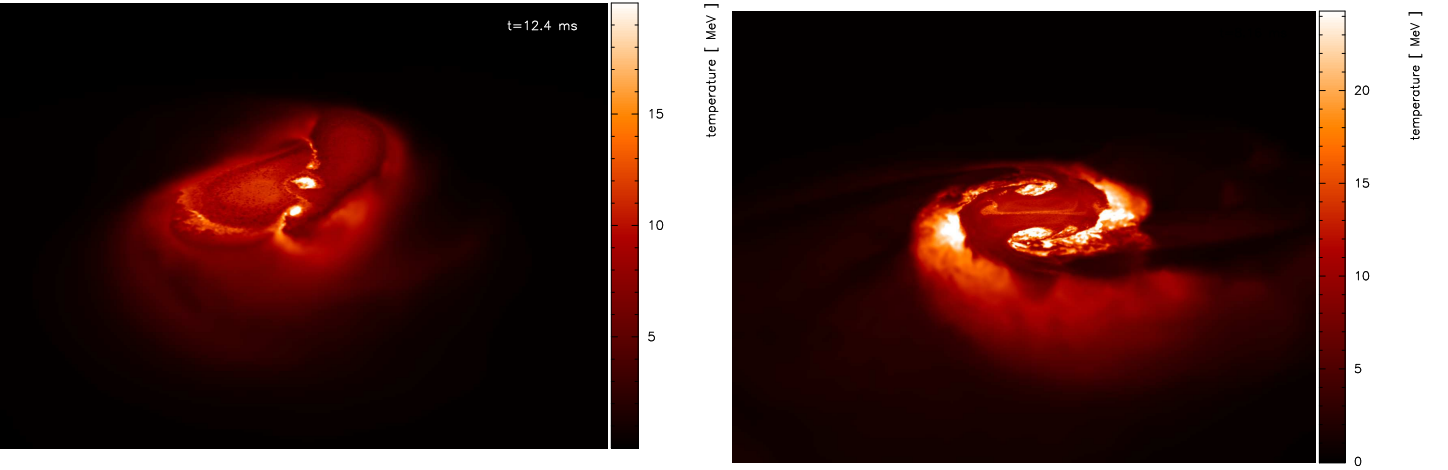


Figure 16. Kelvin-Helmholtz unstable shear interfaces are a natural consequence of ns^2 collision (illustrated here in 3D rendering of the temperature distribution; only matter below orbital plane is shown). Left: grazing impact ($\beta = 1$, run A), right: more central collision ($\beta = 2$, run B), colour bars restricted to $T < 20/24$ MeV to enhance visibility.

ns^2 collisions this value can be exceeded by more than an order of magnitude, see Tab. 3. The engine dynamics leaves a clear imprint in the neutrino luminosity. The oscillations of the freshly formed central remnant of a ns^2 collision show up as ms oscillations in the neutrino luminosities, see Fig. 7, middle panel. In nsbh collisions the core of the neutron star can survive several close encounters. Each of them “re-fills” the accretion disk and thus produces apart from a GW burst also peaks in the neutrino luminosities. We find examples of double peaks where the first occurs

when the ns core impacts on the disk and the second results from the consumption of the “refilled” disk, see for example run E (ns of $1.3 M_\odot$ and bh of $5 M_\odot$), Fig. 7, last panel. If neutrino annihilation should be the main driver for launching relativistic outflows, collisions would be at least as promising as binary mergers. One caveat, though, that applies to both mergers and collisions, is that neutrinos can also deposit part of their energy (either via absorption or annihilation) in the remnant matter and thus drive strong baryonic winds (Dessart et al. 2009). The latter work

found that for at least as long as the central neutron star has not yet collapsed into a black hole a strong baryonic wind is blown along the original rotation axis which may prevent relativistic outflow from forming. This threat may be specific for cases where a central neutron star survives for many dynamical time scales. In such cases neutrinos deposit energy in the outer neutron star layers and thus blow off baryons, see Fig. 10 in Dessart et al. (2009). To which extent this effect also occurs in nsbh encounters is currently not known. This interesting topic certainly deserves more detailed work in the future.

Fallback and late-time activity

A particularly attractive feature of the collision hypothesis is the possibility to launch large amounts of matter into eccentric “fallback” orbits. Collisions can deliver more than twice the fallback mass of the standard neutron star merger case, see Tab. 2. Our fallback plus thick disk accretion model shows time scales in excess of 10^2 s, but it is too simple to account for possible flares. Generally, $\dot{M}c^2$ has dropped below 10^{48} erg/s at times beyond 10^2 s. An intriguing possibility, though, is the survival of the neutron star core in nsbh collisions. In all investigated cases it survives at least the first encounter, in one calculation even three of them and is finally ejected with $\sim 0.1 M_\odot$ in a close-to-parabolic orbit. The interaction with the debris from previous passages may actually brake the core enough to fall back to the bh. This would trigger an impulsive accretion event with $\sim 10^{52}$ erg at possibly very late times. Such scenarios may be responsible for the observed late-time activity in some cases, but they are probably too rare (see below) to account for extended emission in a substantial fraction of sGRBs.

Detectability of the neutrino signal

Most of the energy of both mergers and collisions escapes as ~ 15 MeV neutrinos. The neutrino signature is comparable in magnitude and duration to the signals of a typical core collapse supernova, though dominated by electron antineutrinos. Current facilities can only detect individual neutrino events from within the galaxy (or at most events within the local group). Even if more sensitive detectors are built in the distant future it will be difficult to distinguish the very rare merger or collision events among the much more frequent signals from core collapse SNe. So the neutrinos from compact object encounters may just make an individually undetectable $\sim 0.1\%$ contribution to the diffuse neutrino background.

Detectability of the gravitational wave signal

In both mergers and collisions gravitational radiation carries also a significant fraction of the energy, second only to the neutrino signal. The quasi-regular mergers’ chirping signal can be detected up to distances of a few hundred Mpc, they are the prime targets for gravitational radiation detectors like advanced LIGO and Virgo. Since gravitational waves from eccentric binary systems efficiently radiate angular momentum relative to energy, mergers of primordial binaries are expected to occur at practically zero eccentricity. Binaries that have formed dynamically, say in nuclear or globular clusters, however, form at small orbital separations but with large eccentricities and they may not

have enough time to circularize up to merger. Thus, their close-to-encounter orbital dynamics and gravitational wave signal may differ substantially. Initially they produce a series of well-separated, repeated GW bursts that continues for minutes to days. This sequence of bursts gradually transforms into the powerful chirp inspiral signal of an eccentric binary system. Kocsis et al. (2006) found the signal-to-noise ratio for GWs produced in single parabolic passages to be significant only for rather deep encounters where the initial pericentre separation is $r_{p,0} < 6M$, M being the total mass ($G = c = 1$). O’Leary et al. (2009) estimate that nsbh mergers that result from tidal capture binaries in galactic nuclei could be detectable by advanced LIGO type facilities at rates of ~ 1 per year, i.e. they could contribute of order 1 % to the overall detection rate. Since a significant fraction of tidal capture binaries is expected to merge at non-negligible eccentricities their properties are bracketed between those of the quasi-circular binary mergers and the $\beta \sim 1$ collisions that were discussed in this paper. A first attempt to model such high eccentricity mergers has been undertaken by East et al. (2012), further modeling is left for future efforts.

Rate constraints from ejected matter

It had long been suggested that the cold decompression of neutron star material could produce a substantial contribution to the r-process inventory of the Universe (Lattimer & Schramm 1974, 1976; Eichler et al. 1989; Freiburghaus et al. 1999; Rosswog et al. 1999). Core-collapse supernovae are often considered as the “standard” r-process production site, but recent studies suggest that they are seriously challenged in producing the whole observed r-process pattern (Roberts et al. 2010; Fischer et al. 2010; Arcones & Janka 2011) unless very specific SN events are invoked (Winteler et al. 2012). These findings make an alternative/additional r-process production channel more welcome than ever.

Our reference case, a neutron star merger with masses of $1.4 M_\odot$ (run H), ejects $0.014 M_\odot$ of extremely neutron-rich ($Y_e \sim 0.03$) matter, mainly from the outer core with small contaminations from the more proton-rich crust, see Fig. 11. Grazing ns² collisions (run A) eject material with very similar properties, while more central collisions yield substantially higher temperatures/ e^+ -capture rates and therefore larger Y_e values ($Y_e \approx 0.2$), though still very low in comparison to core-collapse SNe. If we assume an average Galactic r-process production rate of $10^{-6} M_\odot$ per year (Qian 2000) we can place robust upper limits on the admissible encounter rates under the assumption that the ejecta are made entirely of r-process nuclei. Our recent study (Korobkin et al. 2012) finds indeed that the dynamic ejecta of ns² and nsbh mergers are excellent candidates for the production sites of the robust heavy r-process pattern with A larger than ~ 120 . If neutron star mergers alone were responsible for all r-process material this would constrain their galactic rate to $7 \times 10^{-5} M_\odot \text{ yr}^{-1}$, right in the centre of the 95% confidence interval derived from the observed ns² binary distribution (Kalogera et al. 2004), see Fig. 17. Within the given uncertainties they would be perfectly consistent with delivering a substantial contribution to the

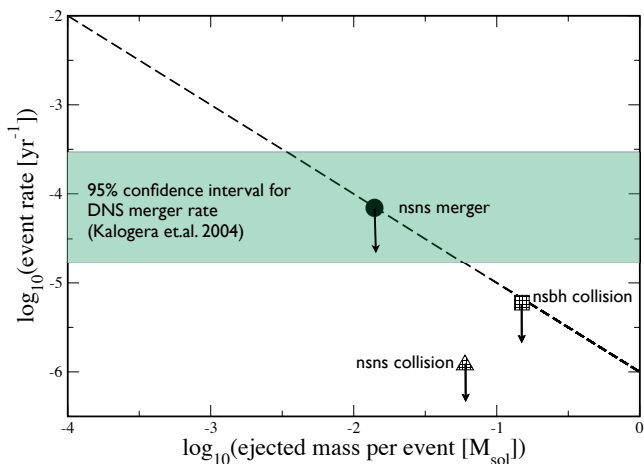


Figure 17. Nucleosynthetic constraints on the event rates. The double neutron star merger rate that is required in order to produce all the r-process material (using the average rate of $10^{-6} M_{\odot} \text{ yr}^{-1}$, dashed line, Qian 2000) is marked by the filled circle. This rate is promisingly consistent with the rate derived from observations by Kalogera et al. (2004) shown as green band. If we make the (extreme) assumption that only ns^2 and nsbh collisions produce all the r-process and their relative ratio is 1:5 (Lee et al. 2010) we can place upper limits on their occurrence rates. These limits are marked as triangle (ns^2) and square (nsbh). The rates realized in nature might be substantially below these values.

galactic r-process matter⁶. The collision cases with their larger ejection yields, however, are seriously constrained in their allowed occurrence rates. If we make the extreme assumption that ns^2 and nsbh collisions produce all the r-process and use a nsbh rate, $R_{\text{coll,nsbh}}$, that is five times larger than the ns^2 collision rate $R_{\text{coll,ns}^2}$ (Lee et al. 2010), we find upper limits of $R_{\text{coll,ns}^2} < 1.2 \times 10^{-6} \text{ yr}^{-1}$ and $R_{\text{coll,nsbh}} < 6 \times 10^{-6} \text{ yr}^{-1}$. Therefore the total ($\text{ns}^2 + \text{nsbh}$) collision rate must be $R_{\text{coll}} < 7.2 \times 10^{-6} \text{ yr}^{-1}$, or about 10% of the double neutron star merger rate. Given our extreme assumption that no other astrophysical event produces r-process material the true rate is likely substantially below this estimate.

Macronovae

We estimate the properties of the electromagnetic transients due to radioactive decays for spherically symmetric outflows. The standard neutron star merger case peaks after ~ 0.4 days with a luminosity of $5 \times 10^{41} \text{ erg/s}$. The other merger cases (ns^2 and nsbh) and the ns^2 collisions peak with higher luminosities, both within a factor of about two in comparison to the standard merger case. The neutron star black hole collisions form a distinct group: they all peak beyond 1 day and are substantially brighter than the standard merger case ($\sim 2 \times 10^{42} \text{ erg/s}$).

Radio signal from ejecta-ISM interactions

⁶ It remains to be investigated, though, to which extent this is consistent with galactic chemical evolution, see e.g. Argast et al. (2004)

In analogy with supernova remnants, the matter that is ejected at sub and mildly relativistic velocities produces a longer lasting radio flare (Nakar & Piran 2011). The flare is the most robust electromagnetic counterpart that is expected from compact mergers or collisions. It depends only on the total energy ejected in mildly or subrelativistic energies and on the density of the external matter. A flare from a canonical ns^2 merger would peak on a time scale of a year with a peak observed flux of $\sim 0.1 \text{ mJy}$ at 1.4 GHz from a source from a distance of 10^{27} cm , roughly the detection horizon of the gravitational radiation signal by the advanced LIGO/Virgo. The signals are longer and weaker if the external density is lower. ns^2 collisions or bhns collisions eject much more material and with a higher velocity and hence the corresponding flares would be stronger and longer. In addition the rise time of these flares will be faster (because of the higher velocities) and hence it will be easier to detect them. In general the rising phase of the flares depends critically on the amount of fastest matter ejected. In these Newtonian calculations we had capped the maximal velocity at $0.75 c$ hence our results on the early emission underestimate the true emission. This part of the relativistic ejecta that we miss in the simulation may produce a brighter and a faster rising signal even if its energy is ten times smaller.

ACKNOWLEDGMENTS

It is a pleasure to thank Almudena Arcones, Brian Metzger, Gabriel Martinez-Pinedo, Oleg Korobkin and B. Sathyaprakash for stimulating discussions. The work of SR was supported by DFG grant RO-3399, AOBJ-584282. This research was supported in part by the National Science Foundation under Grant No. PHY05-25915. Parts of this paper have been written at the University of Queensland, Brisbane, Australia. This visit was supported by the DFG by a grant to initiate and intensify bilateral collaboration. S.R. thanks Enrico Ramirez-Ruiz/UC Santa Cruz and Andrew MacFadyen/NYU for their hospitality and for many stimulating discussions. It is a pleasure to acknowledge the use of the visualization software SPLASH developed by Daniel Price (2007). The simulations of this paper were performed on the facilities of the Höchstleistungsrechenzentrum Nord (HLRN). T.P.'s research was supported by an Advanced ERC research grant. E.N. research was supported by ISF and IRG grants.

Movies from our hydrodynamic simulations and ejecta trajectories can be downloaded from: <http://compact-merger.astro.su.se/>

REFERENCES

- Acernese F., Alshourbagy M., Amico P., Antonucci F., Aoudia S. e. a., 2008, *Classical and Quantum Gravity*, 25, 114045
- Anderson M., Hirschmann E. W., Lehner L., Liebling S. L., Motl P. M., Neilsen D., Palenzuela C., Tohline J. E., 2008, *Physical Review Letters*, 100, 191101
- Arcones A., Janka H.-T., 2011, *A & A*, 526, A160

- Argast D., Samland M., Thielemann F.-K., Qian Y.-Z., 2004, *A&A*, 416, 997
- Arun K. G., Babak S., Berti E., Cornish N., Cutler C., Gair J., Hughes S. A., Iyer B. R., Lang R. N., Mandel I., Porter E. K., Sathyaprakash B. S., Sinha S., Sintes A. M., Trias M., Van Den Broeck C., Volonteri M., 2009, *Classical and Quantum Gravity*, 26, 094027
- Beloborodov A. M., 2008, in M. Axelsson ed., *American Institute of Physics Conference Series Vol. 1054 of American Institute of Physics Conference Series, Hyper-accreting black holes*. pp 51–70
- Benz W., Bowers R., Cameron A., Press W., 1990, *ApJ*, 348, 647
- Bildsten L., Cutler C., 1992, *ApJ*, 400, 175
- Blandford R. D., Znajek R. L., 1977, *MNRAS*, 179, 433
- Bruenn S. W., 1985, *ApJS*, 58
- Burke W. L., 1971, *Journal of Mathematical Physics*, 12, 401
- Burrows D. N., et al. 2005, *Science*, 309, 1833
- Chen W., Beloborodov A. M., 2007, *ApJ*, 657, 383
- Dalal N., Holz D. E., Hughes S. A., Jain B., 2006, *Phys. Rev. D*, 74, 063006
- Dan M., Rosswog S., Guillochon J., Ramirez-Ruiz E., 2011, *ApJ*, 737, 89
- Davies M., Benz W., Piran T., Thielemann F.-K., 1994, *ApJ*, 431, 742
- Demorest P. B., Pennucci T., Ransom S. M., Roberts M. S. E., Hessels J. W. T., 2010, *Nature*, 467, 1081
- Dessart L., Ott C. D., Burrows A., Rosswog S., Livne E., 2009, *ApJ*, 690, 1681
- Duez M. D., 2010, *Classical and Quantum Gravity*, 27, 114002
- East W. E., Pretorius F., Stephens B. C., 2012, *Phys. Rev. D*, 85, 124009
- Eichler D., Livio M., Piran T., Schramm D. N., 1989, *Nature*, 340, 126
- Faber J., 2009, *Classical and Quantum Gravity*, 26, 114004
- Faber J. A., Baumgarte T. W., Shapiro S. L., Taniguchi K., 2006, *ApJL*, 641, L93
- Faber J. A., Rasio F. A., 2012, *ArXiv e-prints*
- Fabian A. C., Pringle J. E., Rees M. J., 1975, *MNRAS*, 172, 15
- Fischer T., Whitehouse S. C., Mezzacappa A., Thielemann F.-K., Liebendörfer M., 2010, *A & A*, 517, A80
- Freiburghaus C., Rosswog S., Thielemann F.-K., 1999, *ApJ*, 525, L121
- Freire P. C., Kramer M., Lyne A. G., Camilo F., Manchester R. N., D’Amico N., 2001, *ApJL*, 557, L105
- Gehrels N., Ramirez-Ruiz E., Fox D. B., 2009, *Annual Review of Astronomy and Astrophysics*, 47, 567
- Gorieli S., Bauswein A., Janka H.-T., 2011, *ApJL*, 738, L32
- Grote H., 2008, *Classical and Quantum Gravity*, 25, 114043
- Hoffman R. D., Woosley S. E., Fuller G. M., Meyer B. S., 1996, *ApJ*, 460, 478
- Hughes S. A., Holz D. E., 2003, *Classical and Quantum Gravity*, 20, 65
- Kalogera V., Kim C., Lorimer D. R., Burgay M., D’Amico N., Possenti A., Manchester R. N., Lyne A. G., Joshi B. C., McLaughlin M. A., Kramer M., Sarkissian J. M., Camilo F. G. B., 2004, *ApJ*, 601, L179
- Kiziltan B., Kottas A., Thorsett S. E., 2010, *ArXiv e-prints*
- Kochanek C., 1992, *ApJ*, 398, 234
- Kochanek C. S., Piran T., 1993, *ApJL*, 417, L17
- Kocsis B., Gáspár M. E., Márka S., 2006, *ApJ*, 648, 411
- Kocsis B., Levin J., 2012, *Phys. Rev. D*, 85, 123005
- Korobkin O., Rosswog S., Arcones A., Winteler C., 2012, *MNRAS*, 426, 1940
- Kulkarni S. R., 2005, *ArXiv Astrophysics e-prints*
- Lattimer J. M., Schramm D. N., 1974, *ApJ*, (Letters), 192, L145
- Lattimer J. M., Schramm D. N., 1976, *ApJ*, 210, 549
- Lee W. H., Ramirez-Ruiz E., 2007, *New Journal of Physics*, 9, 17
- Lee W. H., Ramirez-Ruiz E., López-Cámara D., 2009, *ApJL*, 699, L93
- Lee W. H., Ramirez-Ruiz E., Page D., 2005, *ApJ*, 632, 421
- Lee W. H., Ramirez-Ruiz E., van de Ven G., 2010, *ApJ*, 720, 953
- Li L., Paczyński B., 1998, *ApJL*, 507, L59
- Metzger B. D., Arcones A., Quataert E., Martinez-Pinedo G., 2010, *MNRAS*, 402, 2771
- Metzger B. D., Martinez-Pinedo G., Darbha S., Quataert E., Arcones A., Kasen D., Thomas R., Nugent P., Panov I. V., Zinner N. T., 2010, *MNRAS*, 406, 2650
- Metzger B. D., Piro A. L., Quataert E., 2008, *MNRAS*, 390, 781
- Metzger B. D., Piro A. L., Quataert E., 2009, *MNRAS*, 396, 304
- Monaghan J. J., 1985, *Journal of Computational Physics*, 60, 253
- Monaghan J. J., 1992, *Ann. Rev. Astron. Astrophys.*, 30, 543
- Monaghan J. J., 2005, *Reports on Progress in Physics*, 68, 1703
- Nakar E., 2007, *Phys. Rep.*, 442, 166
- Nakar E., Piran T., 2011, *Nature*, 478, 82
- Narayan R., Paczynski B., Piran T., 1992, *ApJ*, 395, L83
- Norris J. P., Gehrels N., 2008, in M. Galassi, D. Palmer, & E. Fenimore ed., *American Institute of Physics Conference Series Vol. 1000 of American Institute of Physics Conference Series, Prevalence of Extended Emission in Short GRBs*. pp 280–283
- Nousek J. A., et al. 2006, *ApJ*, 642, 389
- Obergaulinger M., Aloy M. A., Müller E., 2010, *A&A*, 515, A30
- O’Leary R. M., Kocsis B., Loeb A., 2009, *MNRAS*, 395, 2127
- Özel F., Psaltis D., Narayan R., Santos Villarreal A., 2012, *ApJ*, 757, 55
- Paczynski B., 1991, *Acta Astron.*, 41, 257
- Perley D. A., Metzger B. D., Granot J., Butler N. R., Sakamoto T., Ramirez-Ruiz E., Levan A. J., Bloom J. S., Miller A. A., Bunker A., Chen H., many more 2009, *ApJ*, 696, 1871
- Phinney E. S., 1989, in Morris M., ed., *IAU Symp. 136: The Center of the Galaxy Manifestations of a Massive Black Hole in the Galactic Center*. p. 543
- Piran T., 2005, *Reviews of Modern Physics*, 76, 1143
- Piran T., Nakar E., Rosswog S., 2012, *e-print arXiv:1204.6242*
- Podsiadlowski P., Langer N., Poelarends A. J. T., Rappaport S., Heger A., Pfahl E., 2004, *ApJ*, 612, 1044
- Price D., Rosswog S., 2006, *Science*, 312, 719

- Price D. J., 2007, Publications of the Astronomical Society of Australia, 24, 159
- Qian Y.-Z., 2000, ApJL, 534, L67
- Rasio F. A., Shapiro S. L., 1999, Classical and Quantum Gravity, 16, 1
- Rees M. J., 1988, Nature, 333, 523
- Roberts L. F., Kasen D., Lee W. H., Ramirez-Ruiz E., 2011, ApJL, 736, L21
- Roberts L. F., Woosley S. E., Hoffman R. D., 2010, ApJ, 722, 954
- Rossi E. M., Begelman M. C., 2009, MNRAS, 392, 1451
- Rosswog S., 2005, ApJ, 634, 1202
- Rosswog S., 2007a, MNRAS, 376, L48
- Rosswog S., 2007b, Rev. Mex. Astron. Astrophys., 27, 57
- Rosswog S., 2009, New Astronomy Reviews, 53, 78
- Rosswog S., 2011, in Proceedings of Science, 11th Symposium on Nuclei in the Cosmos Vol. PoS(NIC XI)032, Compact binary mergers: an astrophysical perspective
- Rosswog S., 2012, Philosophical Transactions A, arXiv:1210.6549
- Rosswog S., Davies M. B., 2002, MNRAS, 334, 481
- Rosswog S., Davies M. B., Thielemann F.-K., Piran T., 2000, A&A, 360, 171
- Rosswog S., Liebendörfer M., 2003, MNRAS, 342, 673
- Rosswog S., Liebendörfer M., Thielemann F.-K., Davies M., Benz W., Piran T., 1999, A & A, 341, 499
- Rosswog S., Price D., 2007, MNRAS, 379, 915
- Rosswog S., Ramirez-Ruiz E., Davies M. B., 2003, MNRAS, 345, 1077
- Rosswog S., Ramirez-Ruiz E., Hix W. R., Dan M., 2008, Computer Physics Communications, 179, 184
- Rosswog S., Speith R., Wynn G. A., 2004, MNRAS, 351, 1121
- Ruffert M., Janka H., Schaefer G., 1996, A & A, 311, 532
- Ruffert M., Janka H., Takahashi K., Schaefer G., 1997, A & A, 319, 122
- Schwab J., Podsiadlowski P., Rappaport S., 2010, ApJ, 719, 722
- Shakura N. I., Sunyaev R. A., 1973, A & A, 24, 337
- Shen H., Toki H., Oyamatsu K., Sumiyoshi K., 1998a, Nuclear Physics, A 637, 435
- Shen H., Toki H., Oyamatsu K., Sumiyoshi K., 1998b, Progress of Theoretical Physics, 100, 1013
- Shibata M., Taniguchi K., 2011, Living Reviews in Relativity, 14, 6
- Smith J. R., 2009, Classical and Quantum Gravity, 26, 114013
- Thorsett S., Chakrabarti D., 1999, ApJ, 7512, 288
- Valentim R., Rangel E., Horvath J. E., 2011, MNRAS, p. 409
- van den Heuvel E. P. J., 2004, in V. Schoenfelder, G. Litchi, & C. Winkler ed., 5th INTEGRAL Workshop on the INTEGRAL Universe Vol. 552 of ESA Special Publication, X-Ray Binaries and Their Descendants: Binary Radio Pulsars; Evidence for Three Classes of Neutron Stars?, p. 185
- van Loon J. T., Stanimirović S., Evans A., Muller E., 2006, MNRAS, 365, 1277
- Willke B., Ajith P., Allen B., Aufmuth P., Aulbert C., Babak S., Balasubramanian R., 2006, Classical and Quantum Gravity, 23, 207
- Winteler C., Käppeli R., Perego A., Arcones A., Vasset N., Nishimura N., Liebendörfer M., Thielemann F.-K., 2012, ApJL, 750, L22

This paper has been typeset from a \TeX / \LaTeX file prepared by the author.